LBL-2607
c.2

A MEASUREMENT OF THE POLARIZATION PARAMETER FOR THE REACTION $\pi^- p \to \pi^0 n$ BETWEEN 1.03 AND 1.79 GeV/c

Stephen R. Shannon
(Ph. D. Thesis)

May 1974

Prepared for the U. S. Atomic Energy Commission
under Contract W-7405-ENG-48

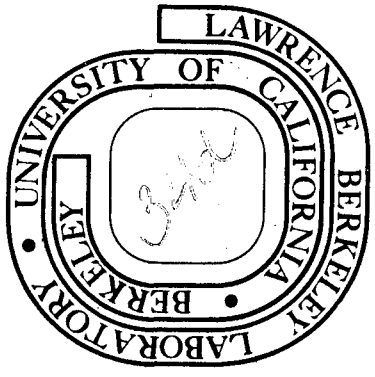

LBL-2607
c.2

DISCLAIMER

A MEASUREMENT OF THE POLARIZATION PARAMETER

FOR THE REACTION $\pi^- p \to \pi^0 n$ BETWEEN 1.03 AND 1.79 GeV/c

Contents

A MEASUREMENT OF THE POLARIZATION PARAMETER FOR THE REACTION $\pi^- p \to \pi^0 n$ BETWEEN 1.03 AND 1.79 GeV/c *

Stephen R. Shannon

Lawrence Berkeley Laboratory
University of California
Berkeley, California 94720

Abstract

Measurements of the polarization parameter for the reaction $\pi^- p \to \pi^0 n$ were made at the five momenta 1.03, 1.245, 1.44, 1.59 and 1.79 GeV/c. A polarized target was used, with polarizations achieved ranging from 48% to 57%. Salient features of the experiment were the use of neutron counters for time-of-flight measurements as well as angular information and the use of optical spark chambers, seven to eight radiation lengths thick, for the detection of the γ rays from the decay of the π^0. The center-of-mass angular range covered by the 20 neutron counters was typically $-.78 < \cos\theta_{c.m.} < .87$. For each momentum there are approximately 10,000 events which fit $\pi^- p \to \pi^0 n$ with a confidence level of at least 10%.

*Work done under the auspices of the U.S. Atomic Energy Commission.

I. INTRODUCTION

In this experiment we measured the polarization parameter in $\pi^- p$ charge exchange scattering at the momenta of 1030, 1245, 1440, 1590, and 1790 MeV/c, and thereby completed the basic set of measurements of the differential cross-section and polarization parameter for the three reactions $\pi^+ p \to \pi^+ p$, $\pi^- p \to \pi^- p$, and $\pi^- p \to \pi^0 n$ in this energy region. The present status of measurements in this energy region are shown in Fig. 1.

The determination of the pion-nucleon scattering amplitudes, which usually are written in the form

$$M_I = F_I \cdot I + iG_I \vec{\sigma} \cdot \hat{n}$$

where I specifies the isospin, I is the 2x2 unit matrix, $\vec{\sigma}$ is the vector operator composed of the 2x2 Pauli spin matrices, $\hat{n}$ is the normal to the plane of scattering, and G_I and F_I are the spin-flip and non-spin-flip amplitudes respectively, has so far been attempted primarily through the use of the phase shift expansion in partial wave angular momentum states. Phase shift analyses generally have at least several possible solutions at a given energy; however, measurements of the charge exchange reaction constrain these solutions strongly.

A computer simulation which was completed prior to the initiation of this experiment, and which used the phase-shift analysis programs (and solutions) of Johnson et al[1], indicated that a measurement of the polarization parameter for $\pi^- p \to \pi^0 n$ at twenty angles spanning the full angular range $0° < \theta_{c.m.} < 180°$, each of which having an uncertainty

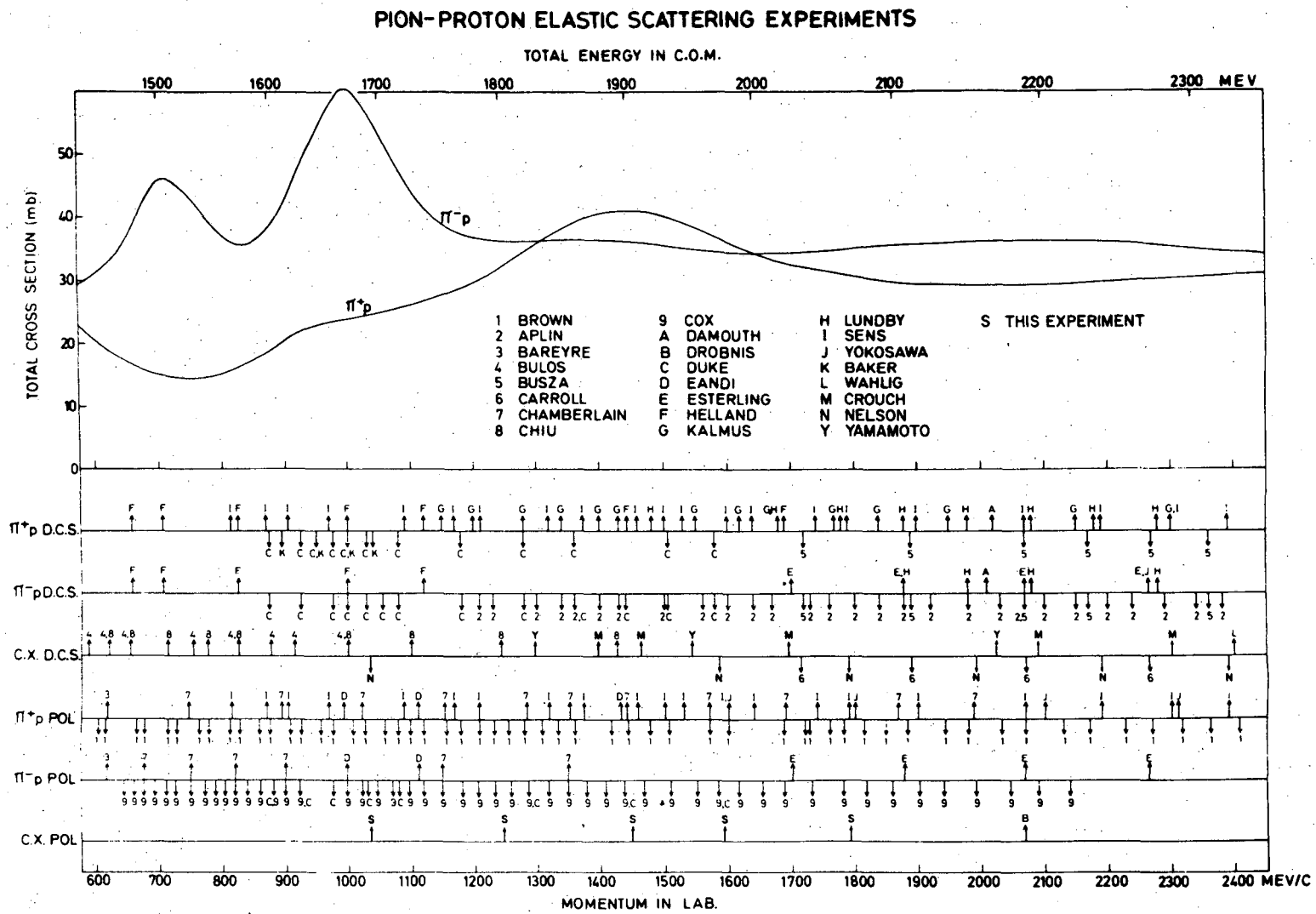

XBL 7312-7236

Fig. 1. Present status of experimental measurements.

Updated version of graph presented in the Proceedings of the Workshop on Particle Physics at Intermediate Energies, from the article Nimrod Experimental Programme, G. Manning, p. 28 (1971).]

of $\delta P = \pm 0.1$, would severely limit the number of acceptable phase-shift solutions. Thus, we hoped to make a significant contribution to the determination of the pion-nucleon scattering amplitudes.

With the completion of measurements of the A and R parameters (discussed in the following section), or some linear combination thereof, there will exist sufficient data to allow direct computation of the amplitudes (both their magnitudes and phases), without relying on phase-shift analysis, provided that the data are of high quality.

II. PHENOMENOLOGY

It is useful to review the phenomenology of the pion-nucleon interaction in order to elucidate the effect of charge-exchange data on the scattering amplitude.

There are four observables which completely describe spin 0-spin 1/2 scattering: the differential cross-section $I_0(\theta)$, the polarization parameter $P(\theta)$, and the two spin rotation parameters $A(\theta)$ and $R(\theta)$ (or linear combinations thereof). The polarization parameter is defined to be the polarization of the outgoing spin 1/2 particle when the spin 1/2 particle in the initial state is unpolarized. The A and R parameters are defined to be the transverse polarization of the outgoing spin 1/2 particle when the initial state spin 1/2 particle is polarized, in the plane of scattering, parallel to and perpendicular to the beam momentum, respectively. (These latter parameters, which are the ones remaining to be measured in this energy region, require a double scattering for their measurement.) Thus, there are twelve observables in pion-proton scattering: I_0, P, A, and R for each of the three reactions discussed above. The effect of each of these parameters in removing ambiguities from the pion-nucleon scattering amplitudes is discussed by Dean and Lee,[2] and by Kelly, Cutkosky, and Sandusky.[3] Since only five of these observables (I_0 for all three reactions, and P for the elastic scattering reactions) have been extensively measured, usually phase-shift analyses have been carried out using expansions of each of the isospin amplitudes in partial wave angular momentum states.

These expansions are:

$$F = \frac{1}{k} \sum_{\ell=0}^{L} \left[\left((\ell + 1)T_{\ell^+} + \ell T_{\ell^-} \right) P_\ell(\cos\theta) \right]$$

$$G = \frac{1}{k} \sum_{\ell=1}^{L} \left[\left((T_{\ell^+} - T_{\ell^-}) \right) P_\ell(\cos\theta) \right]$$

where:

$P_\ell(\cos\theta)$ is the Legendre polynomial of order ℓ,

$P_\ell'(\cos\theta)$ is the associated Legendre polynomial of order ℓ,

L is a cut-off value for the angular momentum,

ℓ^+ means $j = \ell + 1/2$,

ℓ^- means $j = \ell - 1/2$,

$T = \frac{\eta e^{2i} - 1}{2i}$ is a partial wave amplitude, where the η's and the δ's are the phase shift parameters.

Some ambiguities in the present phase-shift solutions for the pion-nucleon scattering amplitudes can be discussed using the method of Barrelet zeroes.[4] This method indicates clearly the importance of high quality charge exchange data for the reduction of the number of acceptable phase-shift solutions. The method depends on the existence of the angular momentum cut-off L in the above expansions, and the resultant reduction of the expressions for F and G to sums of polynomials, hence becoming polynomials themselves. The complex roots of these polynomials are then determined, and used to find the possible ambiguities in the phase-shift solutions, as the following analysis, presented by Gersten,[5] shows.

We introduce the form of the scattering amplitude in terms of the charge amplitudes f_q and g_q (where $q = \pm 1$ refers to $\pi^{\pm}p$ elastic scattering, and $q = 0$ denotes the charge-exchange reaction)

$$M_q = f_q + ig_q\vec{\sigma}\cdot\hat{n}$$

The differential cross-section and polarization parameter for the elastic scattering reactions can be written:

$$I_0^{\pm}(\theta) = |f_{\pm}(\theta)|^2 + |g_{\pm}(\theta)|^2$$

$$I_0^{\pm}(\theta)P^{\pm}(\theta) = -2Imf_{\pm}^{*}(\theta)g_{\pm}(\theta)$$

Since $f(\theta) + ig(\theta) = f(-\theta) - ig(-\theta)$, and defining the amplitude

$$h^{\pm}(\theta) = f_{\pm}(\theta) + ig_{\pm}(\theta)$$

we may rewrite the observables as

$$I_0^{\pm}(\theta) = \frac{1}{2}[|h^{\pm}(\theta)|^2 + |h^{\pm}(-\theta)|^2]$$

$$I_0^{\pm}(\theta)P^{\pm}(\theta) = \frac{1}{2}[|h^{\pm}(\theta)|^2 - |h^{\pm}(-\theta)|^2]$$

Those sets of phase shifts which lead to the same $|h^{\pm}(\theta)|^2$ thus give the same values for $I_0^{\pm}(\theta)$ and $P^{\pm}(\theta)$. The next step is to find a systematic procedure which gives all of those sets of phase shifts which give the same $|h^{\pm}(\theta)|^2$.

Using the expansions of $f_q(\theta)$ and $g_q(\theta)$ to order L in the Legendre and associated Legendre polynomials, respectively, we can expand $h_c(\theta)$ in the more convenient variable $z = \tan(\frac{1}{2}\theta)$, in which variable $h_c(\theta)$ is a polynomial of order 2L. If we can find the roots $\{z_i\}$ of this polynomial, then we may write them as products:

$$h^{\pm} = A^{\pm}\prod_{i=1}^{2L}(z - z_i^{\pm})$$

A replacement of any $z_i^{\pm}$ (or combination of them) by their complex conjugates results in the same value of $|h^{\pm}|^2$, and thus gives the same value for the observables. Since there are 2^{2L} ways of choosing subsets of all these Barrelet zeroes, independently for h^+ and h^-, there are thus 2^{4L} different pairs of amplitudes, all of which predict exactly the same observables. However, the amplitudes obtained by making such Barrelet transformations will often exceed the unitary limit, so the actual number of acceptable ambiguous solutions may be far less.

With the addition of data on charge exchange scattering, we have

$$I_0^0(\theta) = \frac{1}{2}[|h^0(\theta)|^2 + |h^0(-\theta)|^2]$$

$$= \frac{1}{4}[|h^+(\theta) - h^-(\theta)|^2 + |h^+(-\theta) - h^-(-\theta)|^2]$$

$$= \frac{1}{2}(I_0^+ + I_0^-) - \frac{1}{2}Re[h^{+*}(\theta)h^-(\theta) + h^{+*}(-\theta)h^-(-\theta)]$$

Similarly,

$$I_0^0(\theta)P^0(\theta) = \frac{1}{2}(I_0^+P^+ + I_0^-P^-) + \frac{1}{2}Re[h^{+*}(\theta)h^-(\theta) - h^{+*}(-\theta)h^-(-\theta)]$$

Hence, these expressions constitute a constraint on the Barrelet transformations: the observables I_0^0 and P^0 are not invariant under such a transformation, and the Barrelet ambiguities are removed. Of course, in practice, there is error in the data, and the constraints are accordingly weakened. Analyses incorporating recent high quality charge exchange differential cross-section data still have some remaining ambiguities; it is hoped that data from this experiment will improve the situation.

III. EXPERIMENTAL METHOD

A. Summary

This experiment, performed at the Bevatron, resulted in measurements of the polarization parameter $P(\theta)$ in $\pi^- p \to \pi^0 n$ at the five momenta 1030, 1245, 1440, 1590 and 1790 MeV/c. The choice of momenta was based on the existence of rather complete sets of data in the other easily accessible πN scattering parameters; i.e., σ_t for $\pi^{\pm} p$, I_0 for $\pi^{\pm} p \to \pi^{\pm} p$ and $\pi^- p \to \pi^0 n$, and $P(\theta)$ for $\pi^{\pm} p \to \pi^{\pm} p$. In particular, the momenta 1030, 1590 and 1790 MeV/c were chosen to conform to the recent high precision charge-exchange cross-section measurements of Nelson, et al.[6]

The experiment is schematically illustrated in Fig. 2. The negative pion beam impinged on a polarized proton target, which consisted primarily of propylene glycol. Free protons constituted only about 14% of the protons in the target (the rest are protons bound in the carbon and oxygen nuclei of the propylene glycol target, and in the heavier nuclei of the cavity). Hence, a large background from quasi-elastic charge exchange scattering from these bound protons as well as from inelastic scattering was expected. An important feature of the experiment which reduced this background considerably was the detection of both the neutron and the two γ rays from the π^0 decay in order to identify the charge exchange reaction.

Surrounding the target (on all sides as well as top and bottom) was a system of scintillation counters which allowed the identification of those $\pi^- p$ interactions having neutral final states. Those veto counters which were not in the incident beam were also used to veto events which had γ rays emitted in directions other than toward the spark chambers.

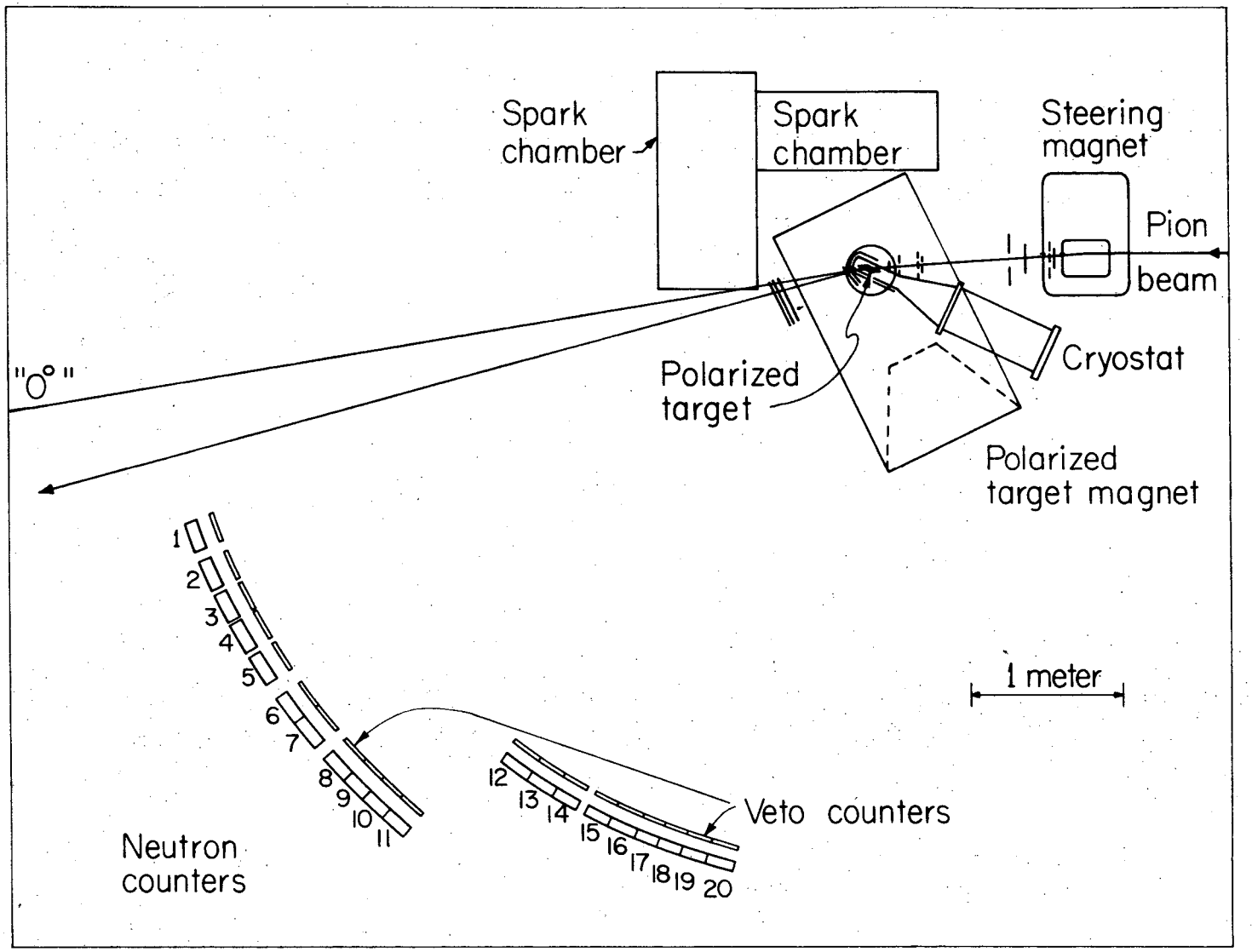

Fig. 2. Experimental layout of polarized target, spark chambers, and neutron detectors.

These counters had scintillator-gamma-converter (1-2 radiation lengths of either lead, tungsten, or platinum) sandwich construction.

The photons from the π^0 decay were detected in two multiplate spark chambers having 8-9 radiation lengths of lead. The chamber plates were made thin ($\sim$0.14 radiation lengths) to ensure a low-energy gamma-ray detection threshold of about 10 MeV. Gamma rays originating at the center of the target were restricted by the magnet aperture to scattering angles normal to the scattering plane of $\pm 21°$.

Neutrons produced in the final state were detected by twenty thick scintillation counters, each of which was further protected from charged particles by a veto counter placed in front of it. In addition, most of these veto counters were shadowed by lead sheets which aided the identification of gamma rays passing toward the neutron counters. These neutron counters, each subtending an angular interval of $\sim 2.5°$, at a distance of $\sim$5 m from the target, effectively spanned the whole angular interval of $0° < \theta_{c.m.} < 180°$ in the center of mass system; furthermore, in conjunction with a counter upstream of the target, they provided time-of-flight measurements.

An event was recorded whenever the following criteria were satisfied: 1) a charged pion went into the target and no veto counter had a pulse; 2) a neutral particle went into one of the neutron counters and was detected there. Data was acquired at a rate of about 5 to 8 events per Bevatron pulse and was usually limited by the cycling time of the camera. On each frame of the film we recorded two 90° stereographic views of each chamber along with a digitized summary of neutron counter number, neutron time of flight,

hodoscope information, target polarization, plus bookkeeping and fiducial information. The film was subsequently scanned for two shower events by professional scanners and physicists. Of these two shower events, those which had neutron time of flight within our timing window, thus becoming candidates for $\pi^- p \to \pi^0 n$, were measured and digitized using the SASS[17] measuring system at LBL. The fitting program SQUAW[21] was used to select those events consistent with charge exchange scattering.

The polarization parameter $P(\theta)$ is calculated from the differential cross-section for the scattering of pions from a polarized proton target:

$$I(\theta) = I_0(\theta)[1 + P_{(\theta)}\vec{P}_t \cdot \hat{n}]$$

where:

$I_0(\theta)$ = differential cross-section for scattering from an unpolarized target at center-of-mass angle θ,

$\vec{P}_t$ = target polarization,

$\hat{n}$ = unit normal to the scattering plane, with the definition $\hat{n} = \dfrac{\vec{k}_i \times \vec{k}_f}{|\vec{k} \times \vec{k}|}$, and $\vec{k}_i$, $\vec{k}_f$ are the initial and final state momenta of the pion in the center-of-mass system.

In this experiment the target was polarized vertically, and the plane of scattering was horizontal, giving $\vec{P}_t \cdot \hat{n} = \pm|P_t|$. Thus, we measure

$$I_{\pm}(\theta) = I_0(\theta)[1 \pm P(\theta)|P_t|].$$

We extract the polarization parameter $P(\theta)$ from a measurement of the asymmetry:

$$\varepsilon(\theta) = \frac{I_+ - I_-}{I_+ + I_-} = P(\theta)P_t$$

Of course, during the course of the experiment the polarization of the target varies (averaging between 50-55%), and the background events contributing to I_+ and I_- had to be subtracted, thus complicating the simple prescription given above. A discussion of these problems will be found in the section on data analysis. To minimize systematic errors, the target polarization was reversed every 2-3 hours. Calibration of the target polarization was made every 3 or 4 days by comparing the natural thermal equilibrium polarization of the protons with the enhanced polarization resulting from applying microwave pumping to the sample.

B. Beam

The pion beam was produced at 0° from an internal alumina target (16.5 cm x 2.5 mm x 6.55 mm) located in the third quadrant of the Bevatron, and transported with a two-stage system of bending magnets and quadrupoles to the experimental area, shown in Fig. 3.

Preliminary studies of the beam were made using the program OPTIK.[7] However, the design of a dispersionless beam focussed onto the relatively small polarized target was greatly simplified by the use of the more detailed program TRANSPORT.[8] The deflection of the beam through the Bevatron magnetic field was calculated with the program BOFUS,[9] using magnetic field values for the third quadrant of the Bevatron magnet which are available from the Magnet Test Group at LBL.

The bending magnet defining the momentum was wire-orbited, with the central momentum of the beam measured to better than 1%. The last two quadrupoles in the beam system were also wire-orbited, mostly as a check on the results of TRANSPORT. Beam tuning was greatly simplified by the use of two multiwire proportional chambers placed near the final focus; histogram and scatter plot displays of the information from the MWPC's were made available on a CRT interfaced with a PDP-5 computer using the program AZTEC;[10] beam profile and phase space scatterplots were also directly displayed on an oscilloscope (without using the PDP-5 as an intermediary). The latter feature allowed continuous adjustment of the beam elements to achieve a small (and circular) focus at the target.

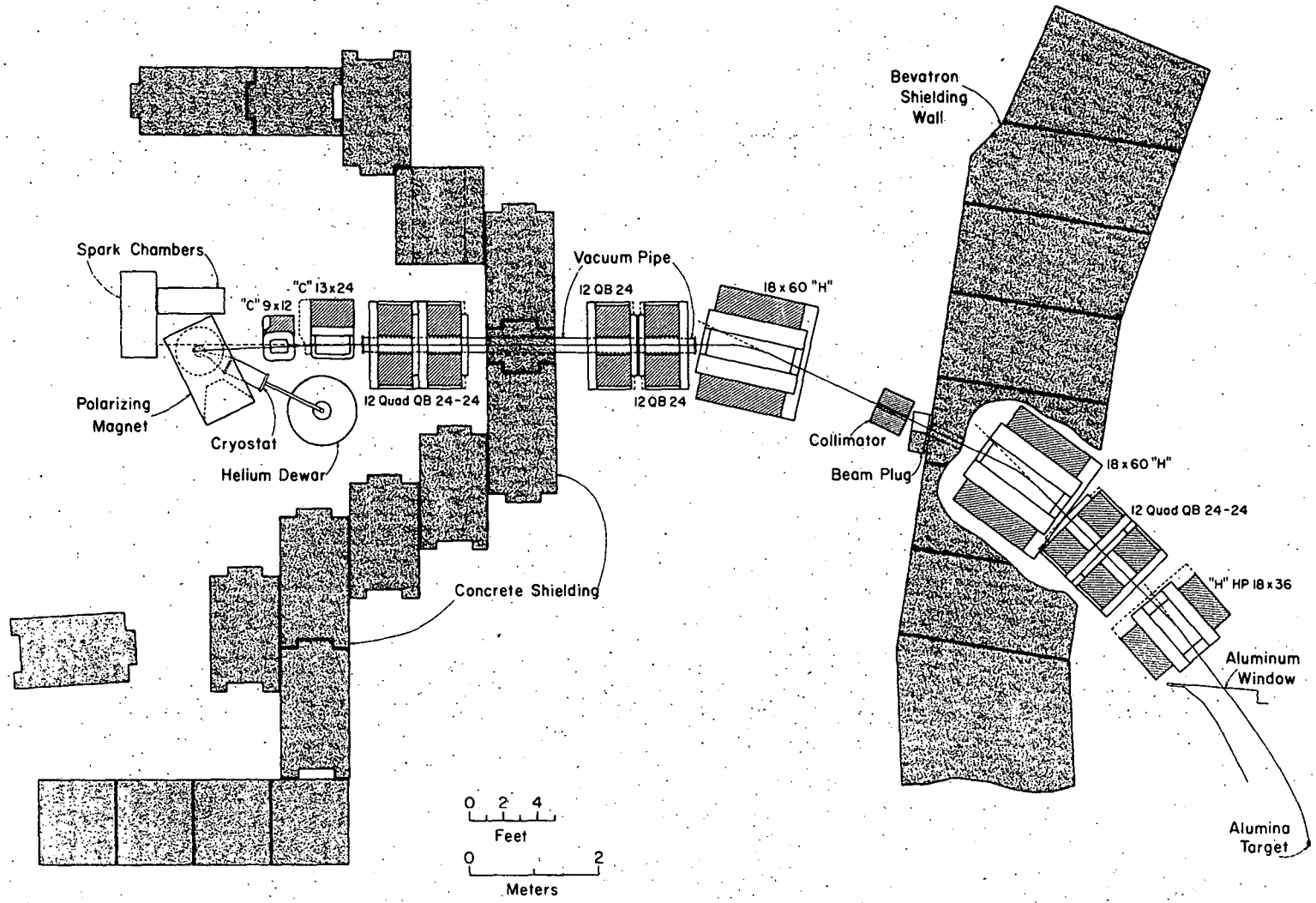

Fig. 3. The eam transport system.

The first stage of the system included a pair of quadrupoles which were used to form a first focus where the momentum selection was done, as well as two bending magnets to deflect the pions from the internal target to that focus. A lead collimator (15 cm long, 20 cm inner diameter) was placed in the first quadrupole to limit the beam size. Another lead collimator, this one with an adjustable slit, was placed at the first focus, specifying the momentum bite and to some extent the flux of the beam. The momentum dispersion caused by the Bevatron field and the first two bending magnets together with the aperture of the collimator was typically $\frac{\Delta p}{p} / \Delta x$ = 0.01/in. The actual momentum spread of the beam ($\sim$1.5%) varied slightly from momentum to momentum, (and even during the course of running at just one momentum, as the aperture was adjusted occasionally to compensate for changes in the flux in the pion beam, due to slight changes in the intensity of the Bevatron proton beam.) Helium bags were used throughout the first leg of the system, and a helium bag and vacuum pipe employed in the second leg of the system to minimize the scattering of the pions along the beam line.

The first focus was followed by the momentum defining bending magnet and two pairs of quadrupoles which focussed the beam onto the polarized target. Additionally, two small bending magnets were placed before the polarizing magnet (affectionately named "Zoltan") to center the beam on the polarized target and to control the direction of the beam as it impinged on the target.

The determination of this direction deserved considerable

attention in this experiment. The direction in which the beam travelled as it passed through the center of the target defined the "0° line" (the direction of $\theta = 0°$ scattering). To guarantee that our preset 0° line did indeed coincide with the beam direction at the center of the target, we inserted a small scintillation counter at the position of the target, and placed another scintillation counter approximately 2 meters downstream of the target at a location calculated from an orbit-tracing program (ZOLORB)[11] which used a Zoltan magnetic field map as input data. As an additional check we used another small (2.5 cm in diameter) counter just upstream of the target as well. The magnetic fields of the two small "C" magnets were adjusted so that the beam trajectory was centered through all three counters; thus the condition for the proper lateral shift and entrance angle was satisfied, and the 0° line was achieved.

The beams typically had a horizontal-full width at half maximum of 1.8 cm and a vertical FWHM of 2.0 cm, as measured with a multiwire proportional chamber having 2 mm resolution situated at the eventual position of the target.

The beam intensity averaged about 10^6 pions/pulse; the typical Bevatron spill length was 1.2 sec. Typically about 10% of the beam was vetoed because of the nearly-simultaneous arrival time of two or more particles.

C. Polarized Target

Much of the operation of the polarized target used in this experiment has been described elsewhere.[12] A brief description of the system including some recent changes follows.

High proton polarizations were attained through the use of the method of dynamic nuclear orientation.[13] In this method the target is at low temperature (1°K) and in a high magnetic field (24.75 kilogauss). Microwave pumping at a frequency of 70 Ghz saturates double spin flip transitions involving the proton spins and the spin of a nearby paramagnetic center (Cr^{+5} radical in this experiment). Substantial polarization of the sample occurs if the proton spin relaxation time is slow compared to the relaxation time for the paramagnetic spins.

Uniformity of the polarizing magnetic field in space and time is necessary to preserve the good signal-to-noise ratio of the NMR signal. With the use of a search coil, provided by the Magnet Test Group, magnetic field maps were made. With this information magnet shims were designed and constructed which achieved the spatial uniformity shown in Figs. 4,5. Output voltage from a pair of Helmholz coils placed near the magnet polefaces was used in a feedback circuit in the magnet regulator and completely compensated for the changes in flux ($\sim$5 gauss) due to the pulsing of the Bevatron magnets.

The target consisted of a 98% propylene glycol-2% water mixture (by weight) saturated to a few percent with Cr^{+5} radical (from $K_2Cr_2O_7$). The target preparation procedure was as follows:

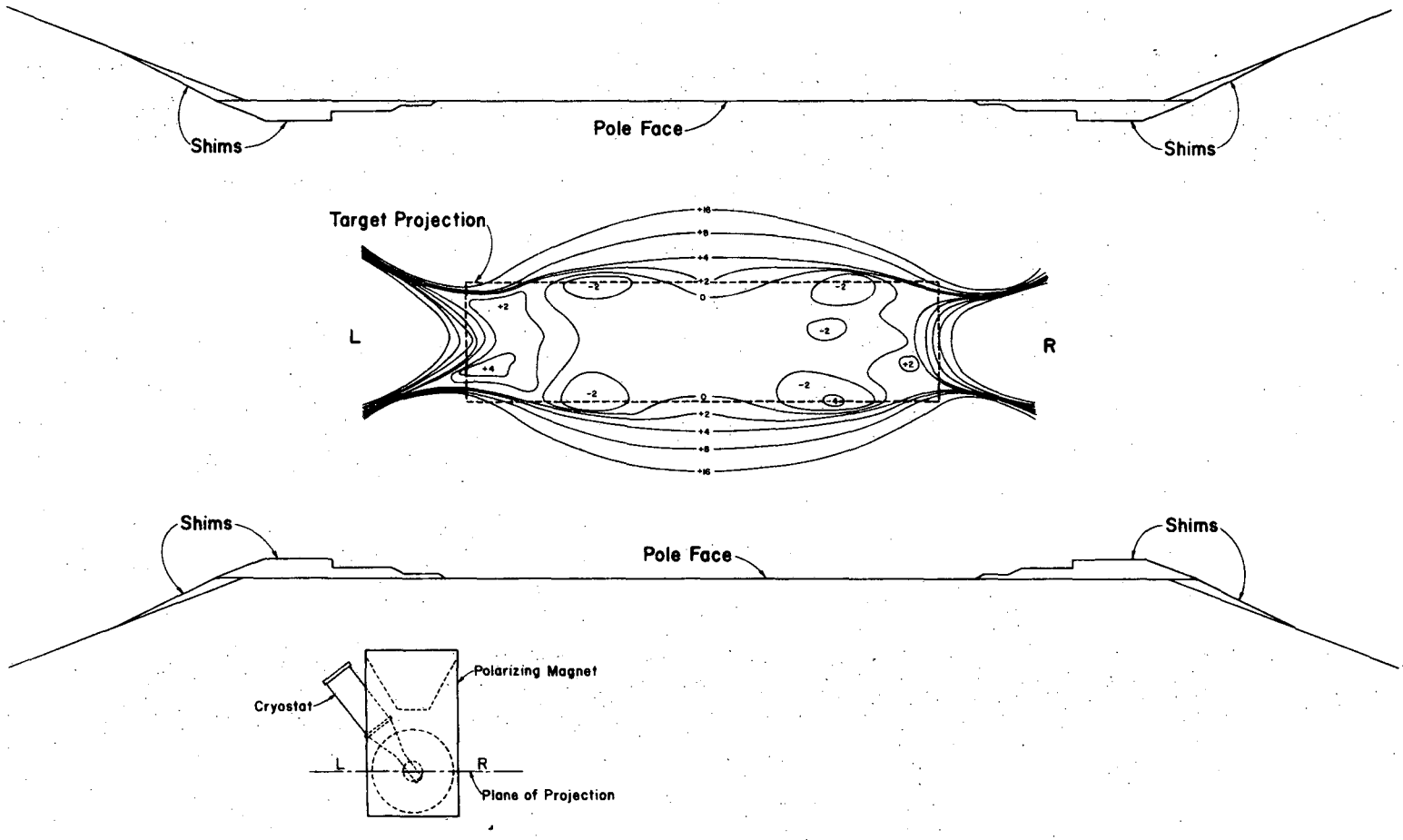

XBL 7312-6826

Fig. 4. Magnet field map of "Zoltan," the polarized target magnet, for the plane of projection indicated in the inset. Contours shown are in gauss, and are the deviations from the nominal value of 24.755 kilogauss. The magnet gap is 11.2 cm.

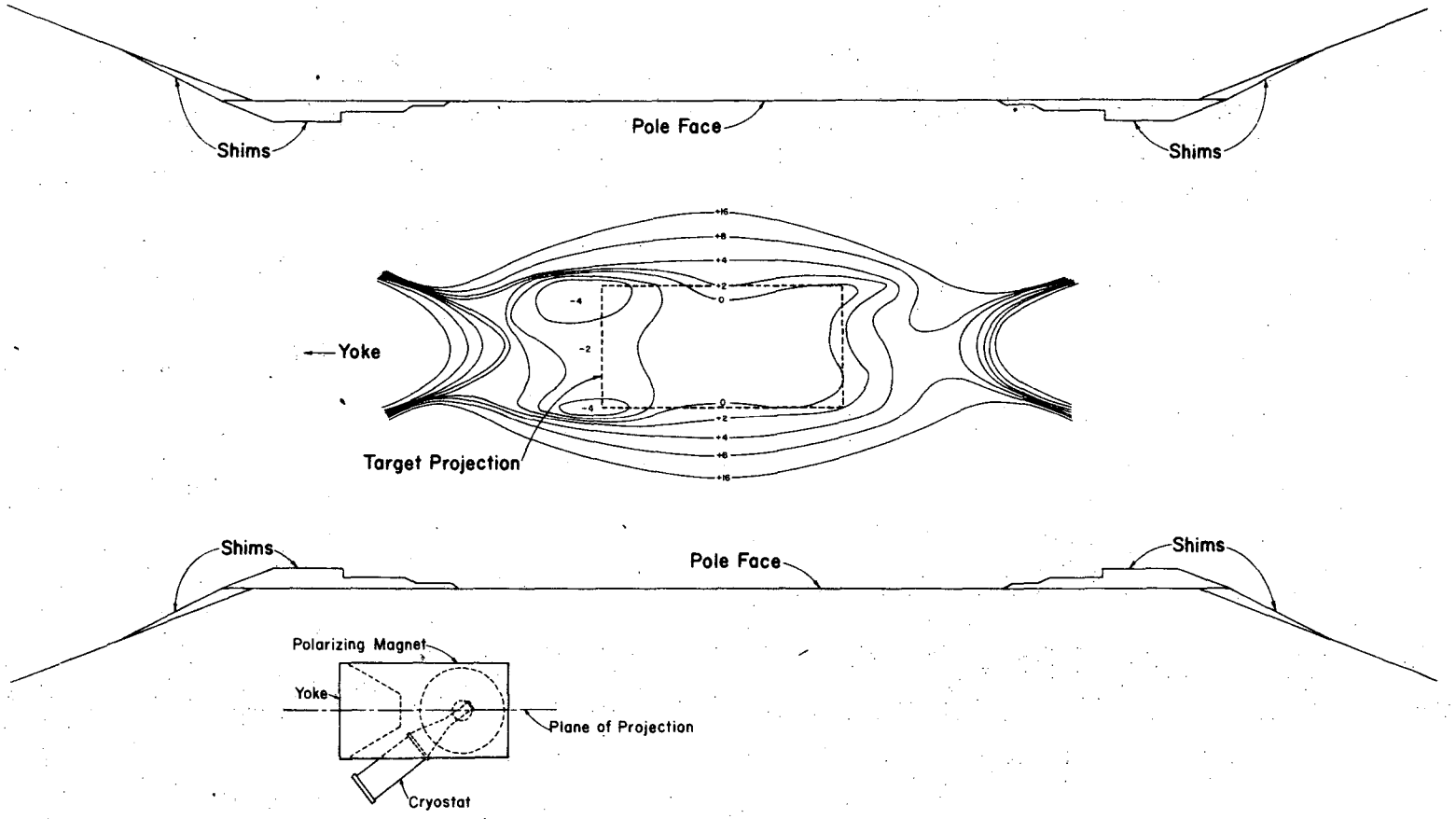

XBL 7312-6827

Fig. 5. Magnet field map of "Zoltan," the polarized target magnet, for the plane of projection shown in the inset. Contours shown are in gauss, and are the deviations from the nominal value 24.755 kilogauss. The magnet gap is 11.2 cm.

(1) bubble nitrogen gas through the propylene glycol (and also the water) for at least three hours, (2) mix the propylene glycol and $K_2Cr_2O_7$ and magnetically stir the mixture for the duration of a 115-minute immersion in a temperature bath at 70°C, (3) cool the mixture for 5 min, and centrifuge for 5 min, (4) carefully remove the supernatent liquid and mix with the appropriate amount of water, (5) seal the resulting mixture into thin-ribbed bags constructed from 12-micron thick FEP Teflon, and (6) quickly place the bags into the microwave cavity. Generally twelve bags were used, giving a typical target weight of about 50 gm. Since the cryostat nose cone was at an angle of 36° to the beam, the target was of rhomboidal form. See Fig. 6. The projection of the target transverse to the beam was 2.5 cm square. The length of the target along the beam direction was 7.5 cm.

The measurement of the target polarization was accomplished through the use of the method of nuclear magnetic resonance. In summary, a weak radio frequency magnetic field (perpendicular to the polarizing field) when applied to the sample near the resonant frequency induced spin-flip transitions of some of the protons. Protons in the target aligned with the polarizing magnetic field area absorbed energy from the rf magnetic field when making transitions; those anti-aligned emitted energy. The target, by absorbing or emitting energy, modified the impedance of the rf circuit driving the rf magnetic field. The detection of this impedance change in a tuned radio frequency circuit was the basis

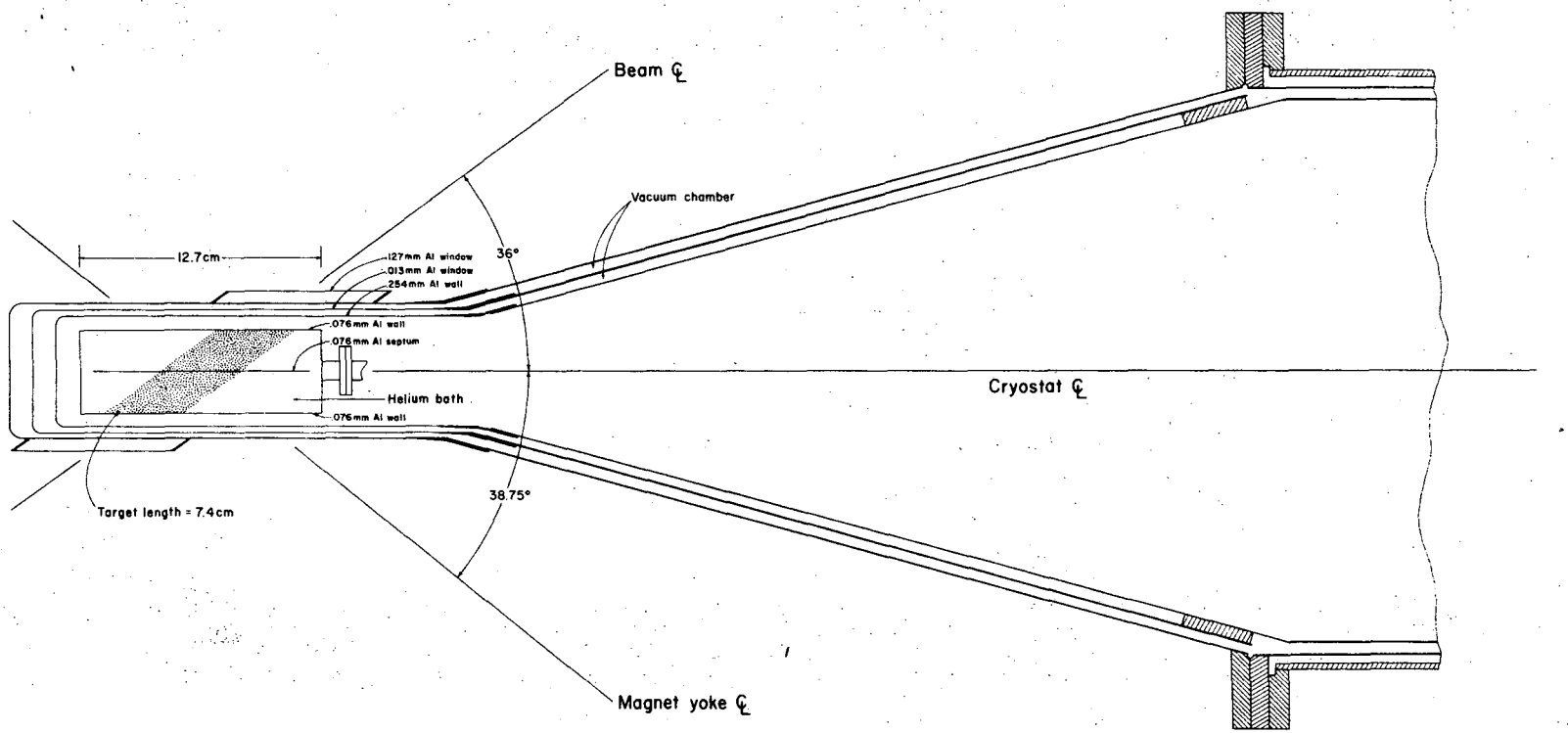

Fig. 6. Detailed layout of the cryostat

of the measurement of target polarization.

The microwave cavity in which the target was placed also served as the part of the rf circuit producing the rf magnetic field. The design of this cavity was changed for this experiment in order to provide a more uniform rf magnetic field (Fig. 7). The cavity was a rectangular copper-plated aluminum box, 13.4 cm long, 3.2 cm high and 3.8 cm wide. A 12.7 cm long, 3.1 cm high, and 0.076 mm thick copper-plated aluminum septum was placed symmetrically along the center line of the long direction, leaving a gap at each end of 3.2 mm. The septum was soldered to the bottom of the box. A folded piece of copper strip ran the length of the box along the top, was soldered to each end of the cavity, and formed a groove into which the septum slid. A 12 micron thick piece of teflon insulated the septum from this strip. A small piece of the septum, called the tab, projected through and was insulated from the strip, so that electrical connection could be made to the septum. The top of the cavity was a fine wire mesh soldered all around the top edges of the box, as well as at two points along the strip $\sim$3 cm on either side of the tab. Rf voltage on the center conductor of a coax cable was applied to the septum tab, while the coaxial shield was soldered to the wire mesh as close as possible to the tab. This arrangement provided us with an rf magnetic field uniform to 5-10% throughout the volume in which the target was placed.

The entire measurement system was calibrated by measuring the polarization of the sample at a known low temperature (in the absence

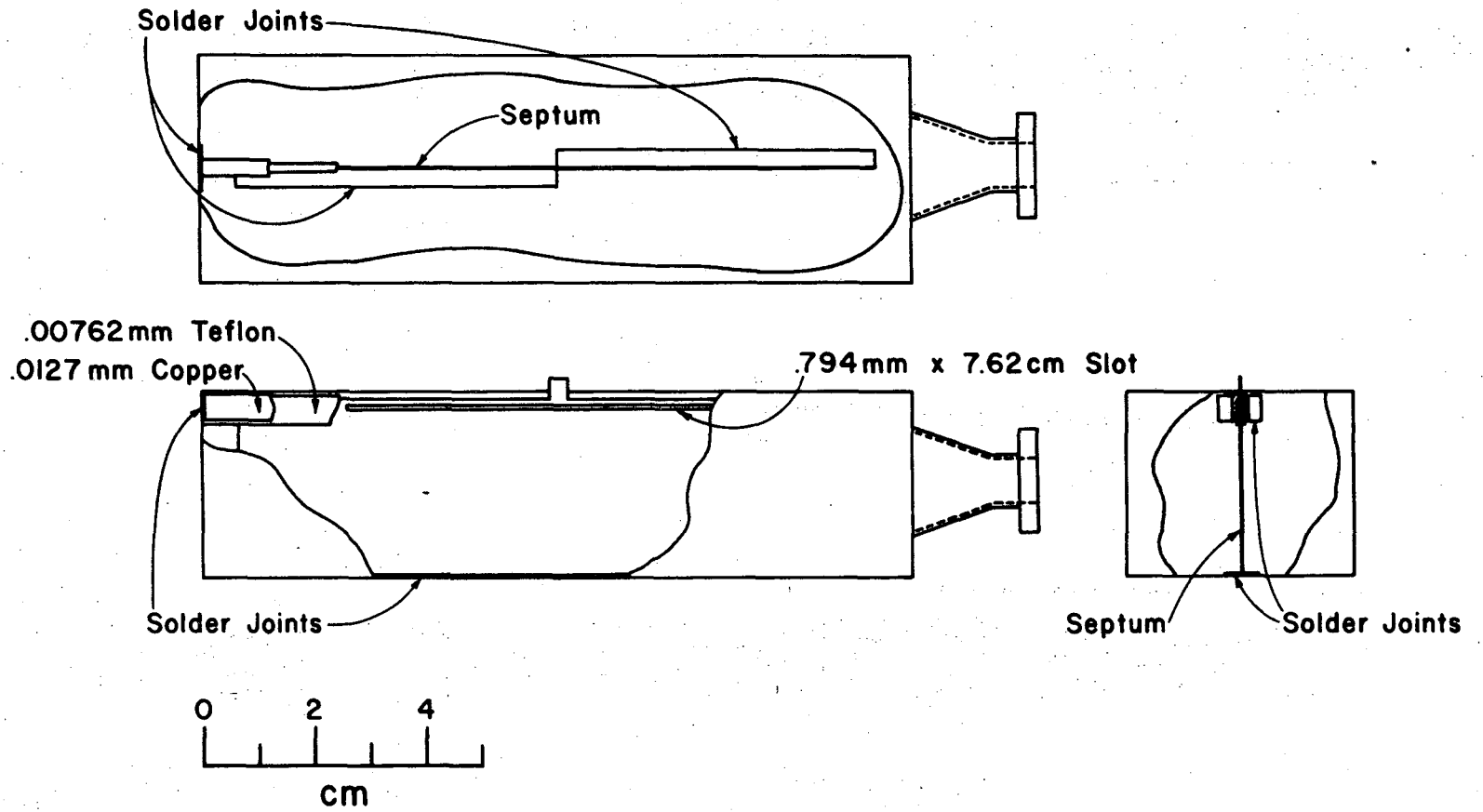

XBL 7312-6894

Fig. 7. Construction details of the microwave cavity.

of microwave pumping, of course). This polarization was calculated from the Boltzmann factor for the populations of the two spin orientations. Calibrated carbon resistors are used for the necessary temperature measurement, while the magnetic field is known from direct measurement, as well as indirectly from nuclear magnetic resonance. Calibration of the sample was made every 3 to 4 days during the experiment. Reversal of the target polarization occurred every 2 to 3 hours. This was done as often as possible to help eliminate systematic errors, yet remain compatible with efficient data-taking.

A PDP-5 computer controlled the NMR detection system, and also, upon command, changed the frequency of the microwave radiation (by changing the high voltage on the "carcinotron" power supply). The polarization measurement system (System 1260) has been extensively described elsewhere.[14] A brief description of the system follows. The computer set the rf frequencies used to sweep the NMR signal and a range of background on either side of the signal. As the rf frequency was swept through the signal, the capacitor in the tuned circuit was also varied so that the circuit was always tuned to a resonant frequency corresponding to the rf frequency. The circuit was kept at resonance, since then the impedance had a particularly simple form, namely, $|Z| = \omega L^2/R$ (neglecting a term of order $1/|Z|$). The output voltage across the tuned circuit was then amplified and converted to a DC level with a diode. This DC level was transmitted to the computer by means of a Voltage-to-Frequency converter. A circuit controlled by the computer converted this frequency to a

number by using 100 of these VFC pulses (the frequencies were ∿100 kHz) to determine the time during which a 100 MHz oscillator is allowed to feed pulses into a scaler. The number in the scaler after it had been gated on and off by the pulses from the VFC was proportional to the inverse of the rf voltage. We used the inverse of the voltage since it is directly proportional to the resistive component of the impedance.

The computer controlled readout completed a sweep through the signal in roughly two seconds, giving us a measurement of the target polarization after every Bevatron pulse. A scaler, with an octal readout of the polarization, in conjunction with an oscilloscope display of the resonance signal allowed continuous monitoring of the system. The target polarization was interfaced to the digitized summary (the "data box") and thus photographed for each event. For part of the running the polarization was also recorded on magnetic tape, as a redundancy check on the data box.

D. Scintillation Counters

The scintillation counters used in the electronic trigger system are shown in Fig. 8. The beam defining counters were M_1, M_2, the seven horizontally defining downstream hodoscope counters 11V, 12V,... 17V, and the counter OB (which had a rectangular hole in its center), used in anticoincidence. Counter M_1 also was the counter which defined the neutron time-of-flight; its RCA 8575 photomultiplier tube had exceptionally low noise, and produced an output pulse which was very stable in time. The counter A_1, in conjunction with A_1', A_5, and A_6, provided a high detection efficiency for charged particles transmitted through the target, although the primary purpose of A_1', A_5, A_6 was the detection of electron showers from gamma rays converted in the lead sheets positioned in front of them. Counters A_2, A_3, A_4, A_{TOP} and A_{BOTTOM} completed the assembly of anticounters surrounding the polarized target, detecting all charged particles leaving the target except those that scattered back up the cryostat. The rectangular hole in the center of counter A_2 shadowed counter M_2, with the resultant vetoing of a few percent of the beam particles passing near the edge of M_2 as well as those which missed M_2 altogether. Counters A_{TOP} and A_{BOTTOM}, with plates of platinum sandwiched between the pieces of scintillator to provide as many radiation lengths of material as possible, also detected gamma rays passing toward the magnet polefaces. These poleface anticounters were shaped to fit the nose cone of the cryostat to take optimal advantage of space limitations. Counter A_4 also had sandwich construction, using

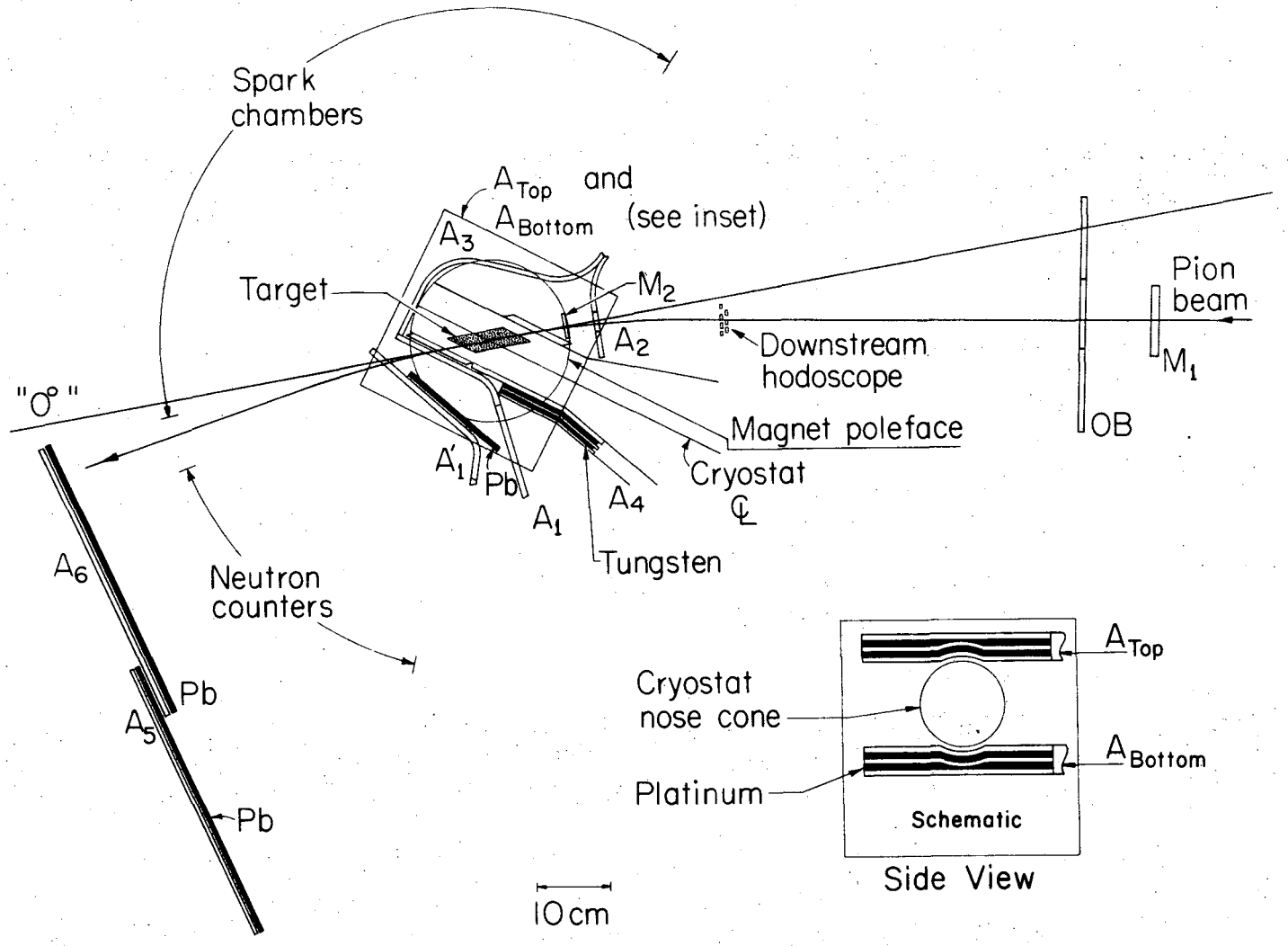

XBL738-3697

Fig. 8. Arrangement of counters near the polarized target. The A_i counters are used in anticoincidence; M_1 and M_2 define the incident beam.

tungsten as the converter, completing the detection system for gamma rays traveling in directions other than toward the spark chambers. All of the afore-mentioned scintillation counters were viewed by RCA-8575 photomultiplier tubes. Specifications for these counters can be found in Table I, along with detailed descriptions of A_4, A_{TOP}, and A_{BOTTOM}. See Fig. 9. (The dimensions of the counters are reluctantly given in English units of length, as they were so designed and constructed.)

Information from an upstream hodoscope, containing five horizontal defining counters 1V, 2V....5V, and three vertical defining counters 1H, 2H, and 3H were recorded on the data box, so that detailed knowledge of the beam direction for each event was available. However, the upstream hodoscope counters were not used in the trigger. These counters also used RCA-8575 photomultiplier tubes.

The twenty neutron counters (N_i) were cylinders of scintillator 8 in. in diameter and 8 in. long viewed by 5 in. diameter Amperex XP-1040 photomultiplier tubes. The counters were placed far enough from the target to give good time-of-flight resolution, yet still have acceptable counting rates. The neutron detection efficiency ($\sim$20%) of these counters was calculated by the method of Kurz,[28] and will be discussed in more detail in a later section. See Table II for the radial and polar coordinates of the neutron counters (the center of the polarized target is the origin of the coordinate system.)

For protection against possible charged particles or gamma rays which passed undetected through the anticounters surrounding the target, veto counters (V_i) were placed over the entrance faces of

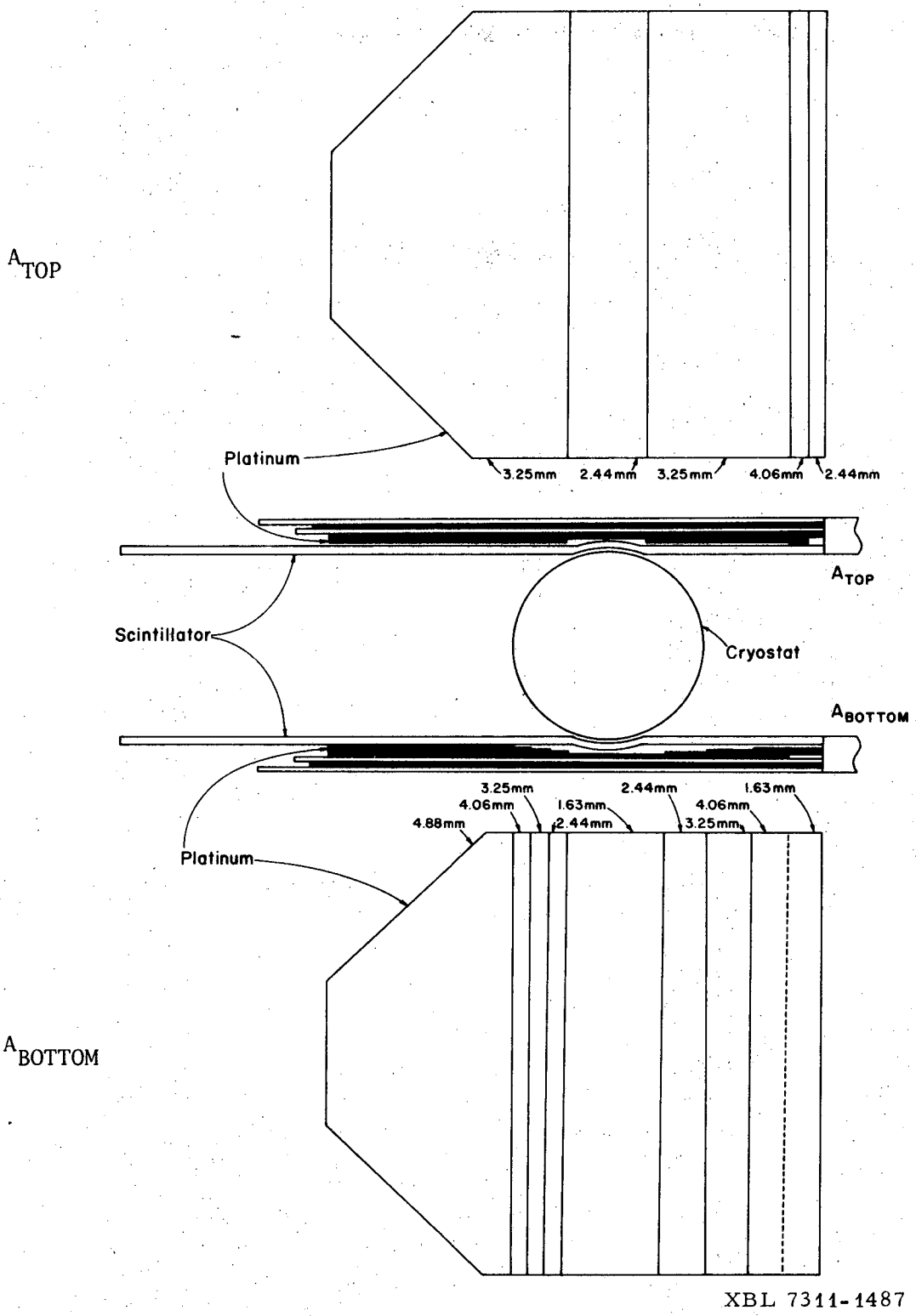

Fig. 9. Construction details for the poleface counters A_{TOP} and A_{BOTTOM} and the anticoincidence counter A_4.

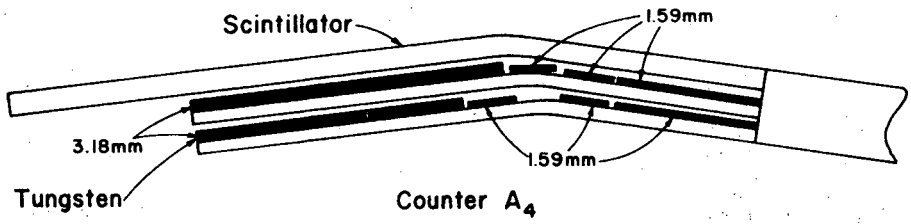

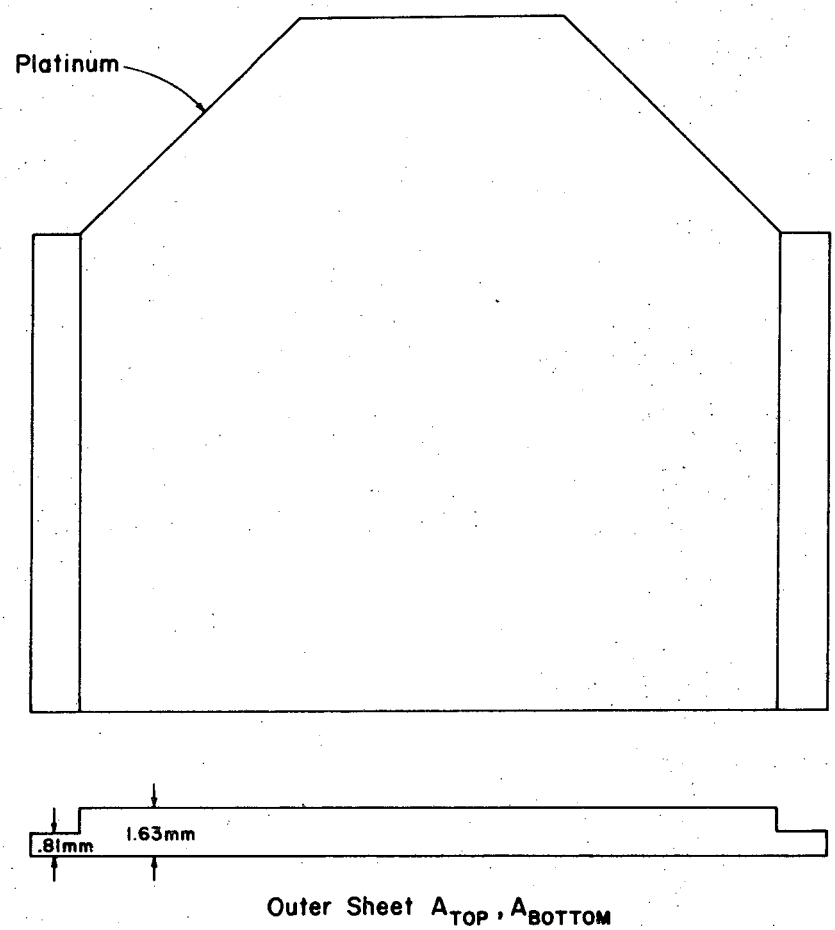

XBL 7311-1488

Fig. 9 (continued).

the neutron counters. Most of these veto counters were covered with 0.25 in. thick lead sheets to convert any gamma rays (spatial limitations precluded the use of the lead for a few of the neutron counters). The veto counters and the lead sheets were 10 in. square.

Table I.

Counter		Dimensions (inches)			Gamma Ray Converter$^{\zeta}$		Distance from Target§	
		Thickness	Height	Width	Material	Approx. Rad. Length		
M_1		.375	2.0	4.0	-	-	34.3	U
M_2		.125	1.25 (diameter)		-	-	5.25	U
A_1		.25	2.5	12.5	-	-	~3.25	D
A_1'		.25	2.5	9.0	Lead	1.1	~6.25	D
A_3		.25	2.5	12.5	-	-	~4.0	
A_5		.25	24.0	15.0	Lead	1.1	24.1	D
A_6		.25	24.0	15.0	Lead	1.1	24.1	D
OB		.25	8.0	12.0	-	-	30.7	U
centred hole			2.0	4.0				
A_2		.25	2.25	4.5	-	-	6.75	U
hole-centre 2^{n} from end of counter			1.25	1.625				
A_4	1†	.25	2.5	8.375	-	-	2.5 - 8	
	2	.125	2.5	6.25	Tungsten	≥.9		
	3	.125	2.5	6.125	Tungsten	≥.9		

Counter$^{\varepsilon}$		Dimensions (inches)				Gamma Ray Converter$^{\zeta}$		Distance from Target
		Thickness	W	L	R	Material	Approx. Rad. Length	
A_{TOP}	1†	.125	8.0	8.0	4.0	-	-	1.375
	2	.0625	7.0	7.5	3.5	Platinum	0.5	
	3	.0625	10.0	10.0	-	Platinum	0.8-2.0	
A_{BOTTOM}	1†	.125	8.0	8.0	4.0	-	-	1.375
	2	.0625	7.0	7.5	3.5	Platinum	0.5	
	3	.0625	10.0	10.0	-	Platinum	0.5-2.0	

Table I (continued).

Hodoscope* Counter(s)	Dimensions (inches)			Overlap	Overall Size	
	Thick-ness	Height	Width		Height	Width
1H, 3H	.125	1.0	5.0	.5	2.5	5.0
2H	.125	1.5	5.0			
1V, 5V	.125	3.5	1.0	.5	3.5	4.5
2V, 3V, 4V	.125	3.5	1.5			
11V, 17V	.0625	1.5	.25	.125	1.5	1.125
12V - 16V	.0625	1.5	.375			

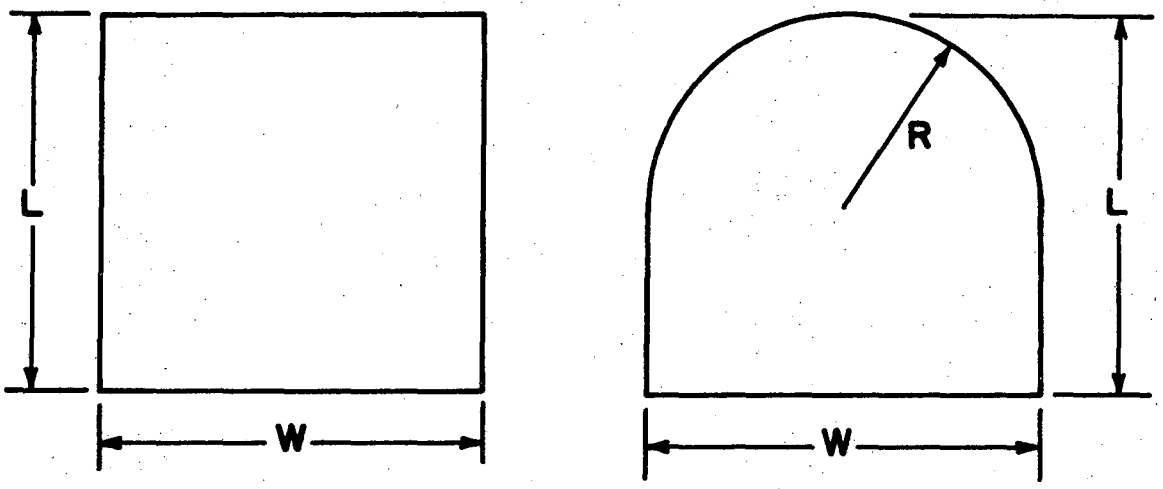

Sheet 1 Sheets 2, 3

Definition of dimensional parameters for A_{TOP} and A_{BOTTOM}

*Upstream hodoscope is 43.56" from target; downstream hodoscope 11.75".

†For those counters with gamma converter-scintillator sandwich construction, sheet 1 is closest to the target, sheet 3 the farthest.

ζThis column refers to material directly in front of the scintillator itself

§Notation: D=downstream, U=upstream; a blank refers to an anticounter not in the beam.

εSee Figure and caption below.

Table II.

Neutron Counter	R† (m)	Polar Angle (θ)	H* (cm)
N_1	4.674	12.06	0.15
N_2	4.681	15.24	-0.15
N_3	4.679	18.22	0.0
N_4	4.641	21.10	0.0
N_5	4.685	23.99	0.0
N_6	4.376	27.72	0.33
N_7	4.688	30.20	0.0
N_8	4.558	33.88	6.99
N_9	4.745	35.85	-6.35
N_{10}	4.971	37.67	6.35
N_{11}	5.007	40.05	-3.81
N_{12}	4.015	45.29	0.97
N_{13}	4.496	47.93	0.33
N_{14}	4.575	50.76	0.33
N_{15}	4.031	54.61	5.87
N_{16}	3.926	57.14	-6.99
N_{17}	3.769	59.72	6.05
N_{18}	3.780	61.80	-10.01
N_{19}	3.753	63.95	5.87
N_{20}	3.833	66.27	20.47

*R is the distance from the center of the target to the center of the neutron counter.

†H is the vertical displacement of the counter from the horizontal plane of scattering (+/- <=> up/down).

E. Electronics

1. Event Defining Electronics

The electronics trigger was designed to register an event when a beam pion interacted in the target with the concomitant detection of a neutral particle in one of the neutron counters, with the constraint that no veto counter had a pulse. Much effort was expended assuring the rate independence of the logic system. We were also careful to have the signal from M_1 determine the timing throughout the system. The electronics system is shown in Fig. 10.

An anode signal from the counter M_1 in coincidence with pulses from M_2 the downstream hodoscope counters, and with a signal from OB in anticoincidence, defined a beam particle. This coincidence signal, which was called B for beam, was then fed into a second coincidence unit MON (monitor) in coincidence with a signal DT (dead time) which did not exist if two or more beam particles arrived close in time to one another. The DT signal originated with a fast M_1 anode signal which was fed into a TR-204A updating discriminator; from this there were two outputs, one with a nanosecond shorted clip to define a short sharp (2 ns) pulse, the other a longer open clip giving a 45 ns long pulse. These two pulses were fed into the coincidence unit DT (free) as shown in Fig. 11. The longer pulse provided a 45 ns veto signal for any signal arriving later. If the two signals arrived closer in time than 25 ns, the earlier signal was also vetoed by virtue of the updating of the open clipped signal. As additional protection against beam particles arriving within $\leq$ 5 ns of each other, the dynode signal

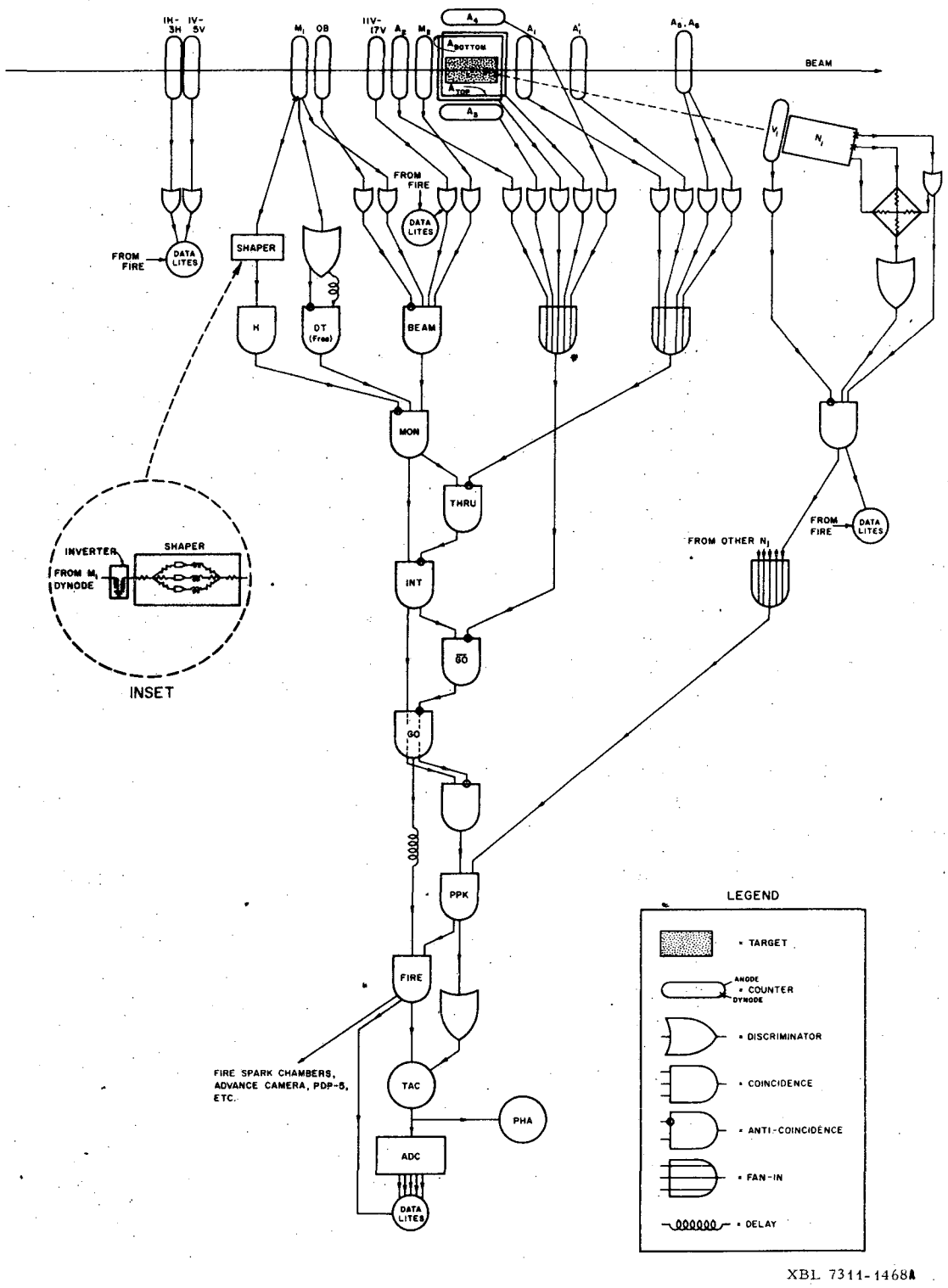

Fig. 10. The electronics.

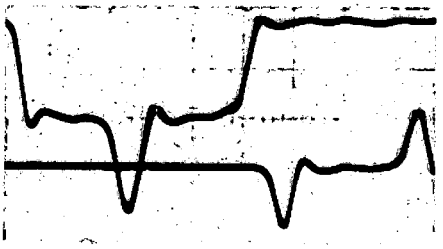

Reproduction of the actual input pulses (from oscilloscope - 10 nsec/large division)

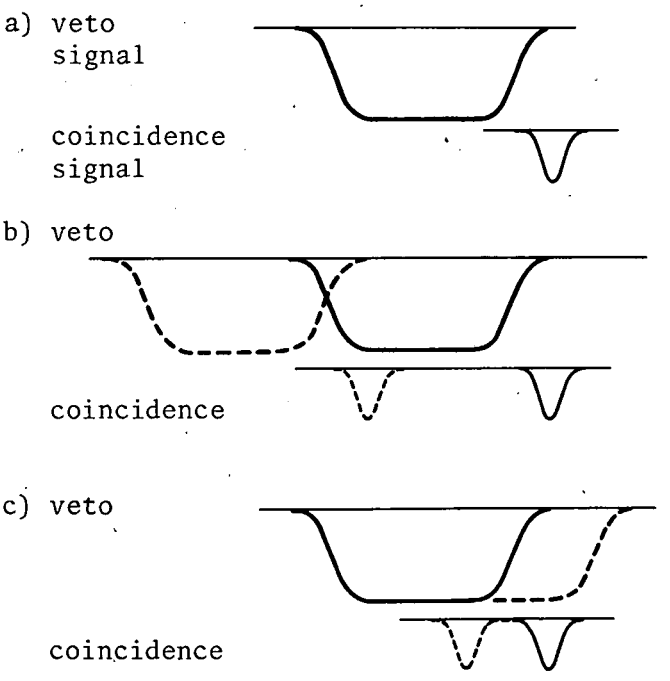

Fig. 11. Inputs to the DT (free) coincidence unit
a) for an isolated M_1 pulse
b) with two M_1 pulses separated by a time 25 nsec < t < 45 nsec.
c) with two M_1 pulses separated by a time t < 25 nsec.

XBB 7312-7362

from M_1 was shaped and then fed into a discriminator with an adjustable threshold. This threshold was set to give an output pulse for the larger integrated input pulse of two charged particles passing through the counter, but not give a pulse for just one incident particle. This signal, H, was then used in anticoincidence in MON. Hence, if two particles arrived within 25 ns of each other, each vetoed the other. If they were within 45 ns of each other, the earlier vetoed the latter. Thus the counting efficiency of the beam signal was rendered rate independent at MON.

To assure rate independence of the complete system, we had only to introduce the anticounters into the logic in a rate independent manner. The anticounters (A_1, A_1', A_5, A_6) were introduced in coincidence with an output from MON at THRU. The output from THRU was then used in anticoincidence with the other output from MON at INT (interact). This procedure allowed us to use a relatively long pulse (16 ns) from the anticounters at THRU, maximizing the anticounter efficiency, yet reducing the rate of anticoincident signals into INT. A similar procedure was used for A_2, A_3, A_4, A_{TOP}, and A_{BOTTOM}, except that the very busy counters A_{TOP} and A_{BOTTOM} were made dead-time free by first putting their signals in coincidence with a pulse from DT. A signal from GO, then, was a beam signal which had no accompanying veto counter pulse. This GO signal, along with a long pulse from one of the neutron counters, and another fast (5 ns) pulse from M_1 which set the timing were fed into the coincidence unit FIRE. A 170 ns pulse from FIRE (the "start" signal) and a 115 ns pulse from the neutron counter (the "stop" signal) were

fed into the time-to-height converter (TAC) and thus to a pulse height analyzer (PHA). The FIRE output was used for a variety of other functions:

1) It triggered the spark chambers, the fiducial lights, the event number lights, and the data box
2) It advanced the camera
3) It generated an 80 msec gate which shut down the system during chamber pulsing and recovery.

FIRE was also put in coincidence with the upstream and downstream hodoscope counters to cause the appropriate lights on the data box to light.

2. Neutron Counter Electronics

The neutron counter system was designed to provide an accurate time-of-flight determination (at least ±1 nsec) along with a measurement of the scattering angle, and to have the highest possible neutron detection efficiency as well. This system, modified slightly for this experiment, was used in prior experiments, and has been described elsewhere.[15]

The neutron counters detected scintillation light produced by a charged particle (usually, a proton) recoiling from an interaction of a neutron with a nucleus in the scintillating medium. Accordingly, there was a broad spectrum of photomultiplier pulses from these neutron interactions, due to the wide variation in energy of the recoil particles. For each counter, the largest pulse was produced by the recoil proton having kinetic energy equal to that of the

incident neutron, provided that the range of that proton was less than the maximum possible path length through the counter. Otherwise, the recoil proton with range equal to the maximum path length produced the largest pulse.

To achieve good timing accuracy when the photomultiplier pulses vary widely in amplitude, the timing of some characteristic point on the pulse must be independent of pulse amplitude over the expected dynamic range. We achieved good timing accuracy in this experiment by using a modified "zero-crossing" timing technique. In this experiment two standard threshold discriminators were used together to simulate a single zero-crossing discriminator. The first, or THRESHOLD, discriminator was used to bias the threshold of the other. The second, or TIMING, discriminator had a threshold of -120 mv. A wide pulse (the "pedestal") of $\sim$-130 mv amplitude was generated by the threshold discriminator and appeared at the timing unit slightly delayed relative to a bipolar pulse from the photomultiplier tube. It was important that the bipolar pulse, which crossed zero from positive to negative amplitude, have an amplitude greater than +130 mv when the pedestal arrived. The threshold of the discriminator was thus $\sim$+10 mv as the bipolar pulse swung from positive to negative polarity. Hence, triggering occurred slightly prior to the point of zero-crossing.

The bipolar pulse from the neutron counter was produced by delaying the anode signal and passively mixing it with an attenuated (3 db) signal from the 14th dynode. At the point of anode-dynode mixing there was also introduced the -130 mv pedestal from the

threshold discriminator. Various combinations of anode delay, attenuation, and triggering level were exhaustively examined to find that combination which minimized time slewing. We typically minimized the slewing to 0.5 nsec over a factor of 8 in pulse height, and 1.2 nsec over a factor of 16.

The pedestal pulse was generated by a second dynode signal. Besides its use in the timing pulse, it was later required in coincidence with the output of TIMING discriminator. A valid neutron count therefore occurred whenever the THRESHOLD discriminator was triggered. The threshold of this discriminator was carefully set and monitored. See Appendix A for details.

An analysis of the "prompt peak" events (e.g., neutron counter events triggered by gamma rays, highly suppressed in this experiment, but still observed), which have $\beta=1$ and thus arrive at a time-of-flight prior to that of the charge exchange events, showed that the FWHM time-of-flight was typically ± 0.6 nsec.

F. Spark Chambers and Optics

The lead plate spark chambers and the associated optical system were used in prior experiments, and were modified slightly for use in this experiment. Detailed descriptions of the spark chambers, spark chamberpulsers, and discharge gaps, and the associated optics are available elsewhere.[16]

The side chamber contained 7 aluminum plates and 42 "lead" plates, each of which was 122 cm square, while the back chamber contained 4 aluminum plates and 60 "lead" plates, each being 152 cm square. The "lead" plates were actually a laminate of 0.40 mm aluminum, 0.80 mm lead, and 0.40 mm aluminum, separated from each other by 7.9 mm thick optically clear lucite frames. The use of such very thin lead plates made the detection efficiency for low energy showers quite good. A large number of such plates were necessary to achieve the considerable thickness in radiation lengths (7 radiation lengths in the side chamber, 9 radiation lengths in the back chamber). The first four plates in each chamber were 1.2 mm aluminum. Gamma rays entering the chambers were unlikely to convert in these plates, since the total thickness was only 0.05 radiation lengths. Thus a particle entering the chamber with a visible track in the first four gaps was thus usually presumed to be charged. The chambers had high multiple spark efficiency and a track sensitive time of about 1.5 μsec. The chambers were fired when the interesting event was about 500 nsec old. A system of field lenses and mirrors brought the four views to a single camera (Flight Research Model #7).

IV. DATA ANALYSIS

A. Film Scanning, Measurement

The reaction $\pi^- p \rightarrow$ (neutrals) almost always gives a neutron + gamma rays in the final state. These gamma rays were detected by converting them to electron-positron pairs and observing the resultant showers in the lead plate spark chambers surrounding the polarized target. The pictures taken were scanned and measured by the LBL Group A scanning and measuring staff.

The film was examined by scanners who recorded the number of showers observed in each picture. Rough coordinates of the first spark of each shower were specified by recording the grid location of the starting point of each shower. The grid gave a spatial resolution of 7.6 cm by 5.1 cm. The showers were also paired in the two stereo views of each chamber. In addition, scanners recorded coordinates for tracks in the spark chambers which were not considered to be valid showers. These included showers with only two sparks, showers that did not point to the polarized target, and showers that might possibly have been fragments from another shower. Almost all of the film taken at each momentum was then scanned and measured by SASS,[17] an automatic measuring system which used a precision cathode ray tube and photomultiplier linked to a PDP-24 computer. SASS read the data box lights, and digitized the positions of all the sparks as well as the fiducials in the same frame. A timing cut, appropriate for each neutron counter, was imposed to eliminate unwanted events and thereby hasten the data analysis (and save money). This timing

window was chosen to be much wider than the width of the charge-exchange peak, and included enough of the tails of the peak to enable us to make a reliable extrapolation of background events. Data from SASS were written on tape with the program FLICKERS.[18]

Using the program mini-DHS,[19] the data from the hand scan was compared with the digitized data from SASS to generate the shower starting point and direction and the number of sparks in the shower. DHS included corrections to take into account distortions due to the mirror-lens system.

The status of each event was stored on a Master List tape, using the program SCALP.[20] Recorded on this tape were the data box information from FLICKERS and the hand scan information, as well as the beam momentum, target condition, and other information bearing on the state of the experimental system.

Using this system, it was found that shower directions had typical uncertainties of ±3° and starting point errors of ±0.75 cm. The angular error was due primarily to the lateral spread of the shower, while the error in the starting point (the first spark) was due to local optical distortions and ambiguities in selecting the first spark in the specified grid zones.

The geometric reconstruction of the event was then performed by a modified version of the LBL Group A fitting program SIOUX.[21] This program calculated the decay point in the target for the interaction, the shower starting points and directions as determined by DHS, and the known target coordinates. Once the decay point was determined, the shower directions were defined by the target decay point and the first spark of the showers.

Table III.

Momentum	Total Pictures	2-Shower Events	Events with C.L. > 5%				
			$\pi^- p \to n\gamma\gamma$	$\pi^- p \to \pi^0 n$	$\pi^- C \to \pi^0 nB$	$\pi^- p \to \eta n$	$\pi^- C \to \eta nB$
1030	359K	47268	36003	12284	32077	36	700
1250	334K	40650	35998	11251	31979	367	1565
1440	344K	48102	39720	16314	33336	235	1089
1590	314K	69943	52853	18345	43564	428	2587
1790	331K	56380	42942	15397	35223	543	2109

Table IV.

Shower Distributions								
	Raw Data				Timing Cut Imposed			
Momentum	0	1	2	≥3	0	1	2	≥3
1030	40.6 %	33.8%	22.5%	3.1%	27.3%	38.7%	31.0%	3%
1245	39.5 %	30.2%	25.9%	4.4%	28.4%	31.8%	35.1%	4.7%
1440	39.9 %	30.5%	26.7%	2.9%	27.1%	32.4%	36.6%	3.9%
1590	30.5 %	25.8%	34.5%	9.2%	18.5%	25.1%	44.1%	12.3%
1790	32.7 %	27.1%	34.6%	5.6%	22.4%	23.8%	46.3%	7.5%

B. Event Identification

Since the polarized protons in the target constituted only about 14% of the protons in the target (the rest are protons bound in the carbon and oxygen nuclei of the propylene glycol, and in the heavier nuclei of the cavity), the expected backgrounds due to quasi-elastic charge-exchange scattering (from these bound protons) and inelastic scattering were estimated in the following way. It should be noted that the scattering of beam pions from neutrons bound in the heavier nuclei do not contribute to the background, except for inelastic reactions (e.g., $\pi^- n \to \pi^- . \pi^0 n$) in which the scattered π^- escapes detection by either being of such low energy as to be absorbed in the target or by exiting the target along the center line of the cryostat (and away from the spark chambers). These reactions were found to give insignificant background contributions.

The program SQUAW fit each event to the hypotheses

I. a) $\pi^- p \to n\gamma\gamma$

b) $\pi^- p \to \pi^0 n$, $\pi^0 \to \gamma\gamma$

c) $\pi^- p \to \eta n$, $\eta \to \gamma\gamma$

II. a) $\pi^- C \to n\gamma\gamma B$

b) $\pi^- C \to \pi^0 n B$, $\pi^0 \to \gamma\gamma$

c) $\pi^- C \to \eta n B$, $\eta \to \gamma\gamma$

where the significant fact about the fictitious particle B and the target particle C is that m_B was chosen such that $m_C - m_B = m_p$, where m_C, m_B, and m_p are the masses of C, B, and the proton, respectively. B may be thought of as a recoil boron nucleus resulting from a quasi-elastic π^- charge-exchange interaction with a proton bound in a carbon nucleus ("C"), but the procedure is valid for π^-

interactions with other nuclei as well. Reactions I.a) and II.a) are 2-C fits, while the others are 3-C fits. Particles B and C were treated as measured particles in the fits, with particle C at rest, and the momentum components of B set equal to zero, with a large uncertainty of ±300 MeV/c. A momentum distribution for particle B was calculated from the fits for reaction II.b) and found to have a half-width of ∿120 MeV/c, characteristic of Fermi motion within a nucleus. Elastic charge exchange events from free protons, as well as quasi-elastic charge exchange from those 'stationary' protons bound in the carbon nucleus should correspond to zero momentum for spectator B, whereas scattering from moving protons and inelastic scattering should correspond to a finite momentum transfer to B. Thus, only those events with small p_B were candidates for the reaction $\pi^- p \to \pi^0 n$.

Fits to $\pi^- p \to \eta n$ were investigated, and events having a confidence level (C.L.) >5% for that reaction were found to constitute less than 1% of those events which fit $\pi^- C \to \pi^0 n B$ (with any C.L.). Thus, backgrounds due to this source are insignificant. This is important, since polarization effects could be observed in such a background. Our veto counter system significantly inhibits the inelastic reactions (e.g., $\pi^- p \to \pi^0 \pi^0 n$) which have more than two gamma rays in the final state. Hence, the predominant contribution to the final state is indeed the quasi-elastic charge exchange reaction. See Table III for a summary of the shower distributions, and Table IV for a summary of the number of events fitting each hypothesis with a C.L. of at least 5%.

Data were taken with dummy targets at each momentum. These

dummy targets, essentially composed of graphite, had an approximately equivalent number of protons/cm^2 as the real target, but consisted only of carbon nuclei to allow a comparison with the above analysis. Polarized target events which fail to fit (C.L. <0.1%) the reaction $\pi^- p \rightarrow \pi^0 n$, but pass (C.L. >10%) the quasi-elastic reaction $\pi^- C \rightarrow \pi^0 nB$ agree very well with the corresponding events from the dummy target, with the normalization ratio being quite consistent with the relative beam fluxes incident on the polarized target and the dummy target. The fitted B momentum distribution for these "failing" events at 1590 MeV/c is shown in Fig. 12. The normalization ratio found above was applied to the events from the dummy target to give the background distribution from the polarized target, also indicated in Fig. 12 along with the total and "passing" events for the beam momentum 1590 MeV/c. There was not enough dummy data to make this estimate separately for each neutron counter; however, the normalization ratios were computed for different groups of neutron counters and were found to be quite consistent with the overall normalization ratio. This overall normalization ratio was used to determine the background for each counter (the failing events for both signs of target polarization are compared to the normalized failing dummy events in Fig. 13). For comparison, the "passing" events along with the estimated background are displayed in Fig. 14.

The event sample used for the calculation of the polarization parameter was the total number of two-shower events taken for each sign of the target polarization, with the extrapolated background subtracted. The method used in calculating the polarization is given

in Appendix B. The polarization parameter was evaluated for each counter using a series of cuts in p_B, and was relatively independent of the value of p_B used. The value of the polarization parameter quoted is the one having minimum error (typically, for $p_B \lesssim 120$ MeV/c).

As a consistency check, the polarization parameter was evaluated using a different method (see Appendix D) based on the neutron time-of-flight distributions of the entire event sample (irregardless of γ-ray multiplicities). The results were in excellent agreement with the values of the polarization parameter found using the above analysis. The values for the most backward scattering angle at 1030, 1440, and 1590 MeV/c quoted in the tables were results from this analysis, as there were very few two-shower events associated with the most forward of the neutron counters.

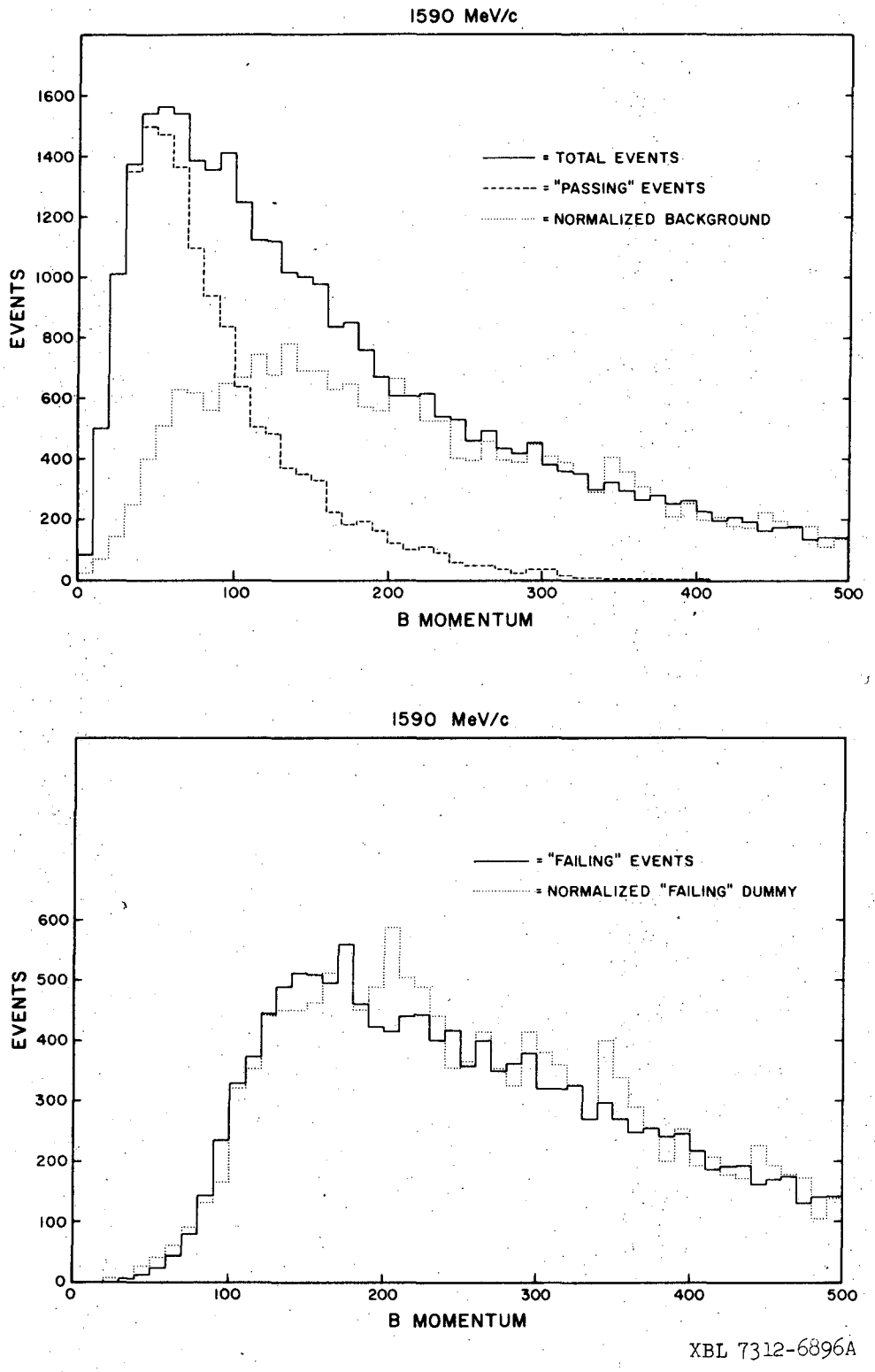

Fig. 12. The distribution of events from the dummy target and the polarized target as a function of p_B. ("Passing" events fit the hypothesis $\pi^- p \rightarrow \pi^0 n$ with a confidence level > 10%, while the "failing" events have confidence level < 0.1%).

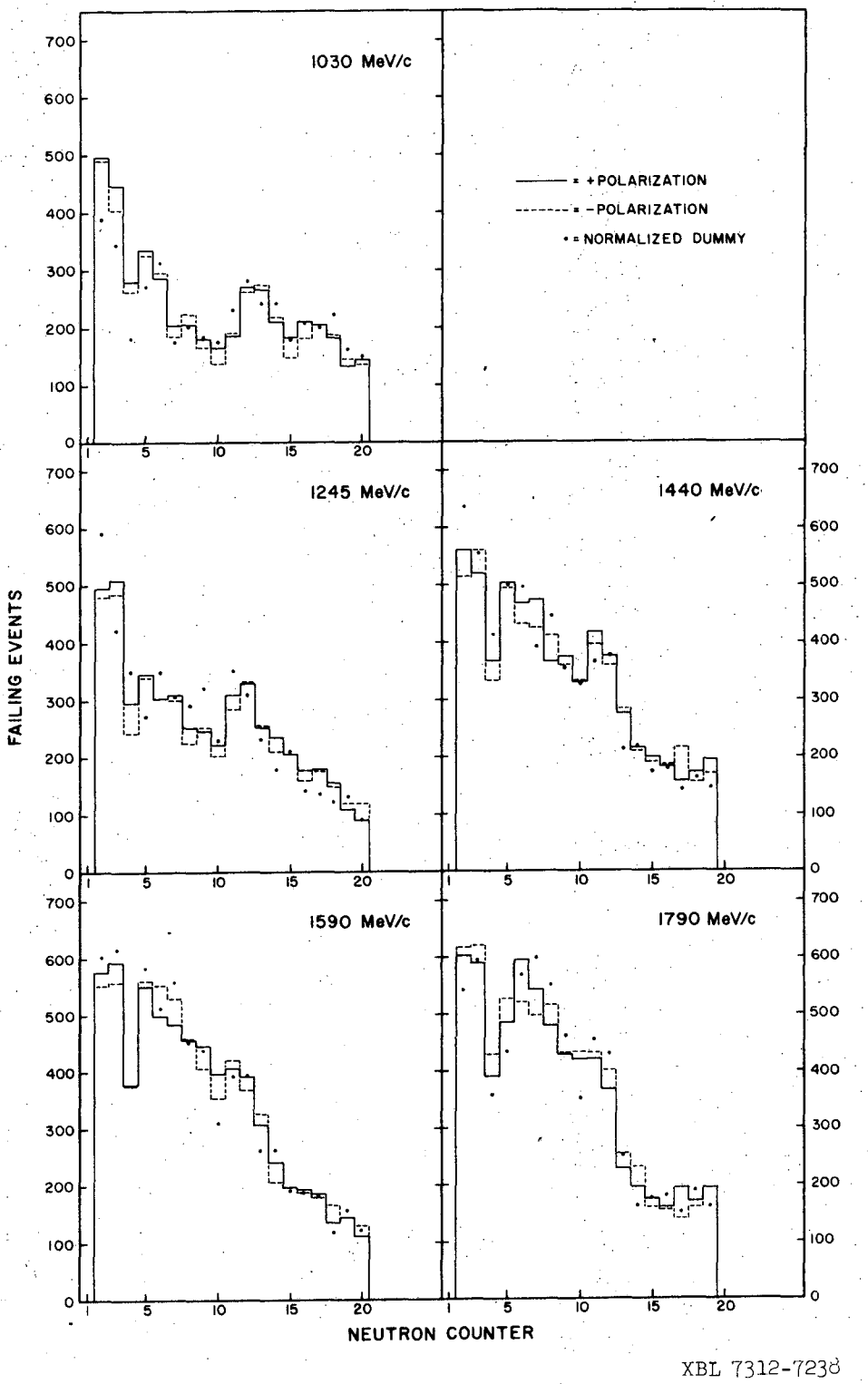

Fig. 13. For each momentum, the failing events from the polarized target are compared with the normalized failing events from the dummy (and with each other).

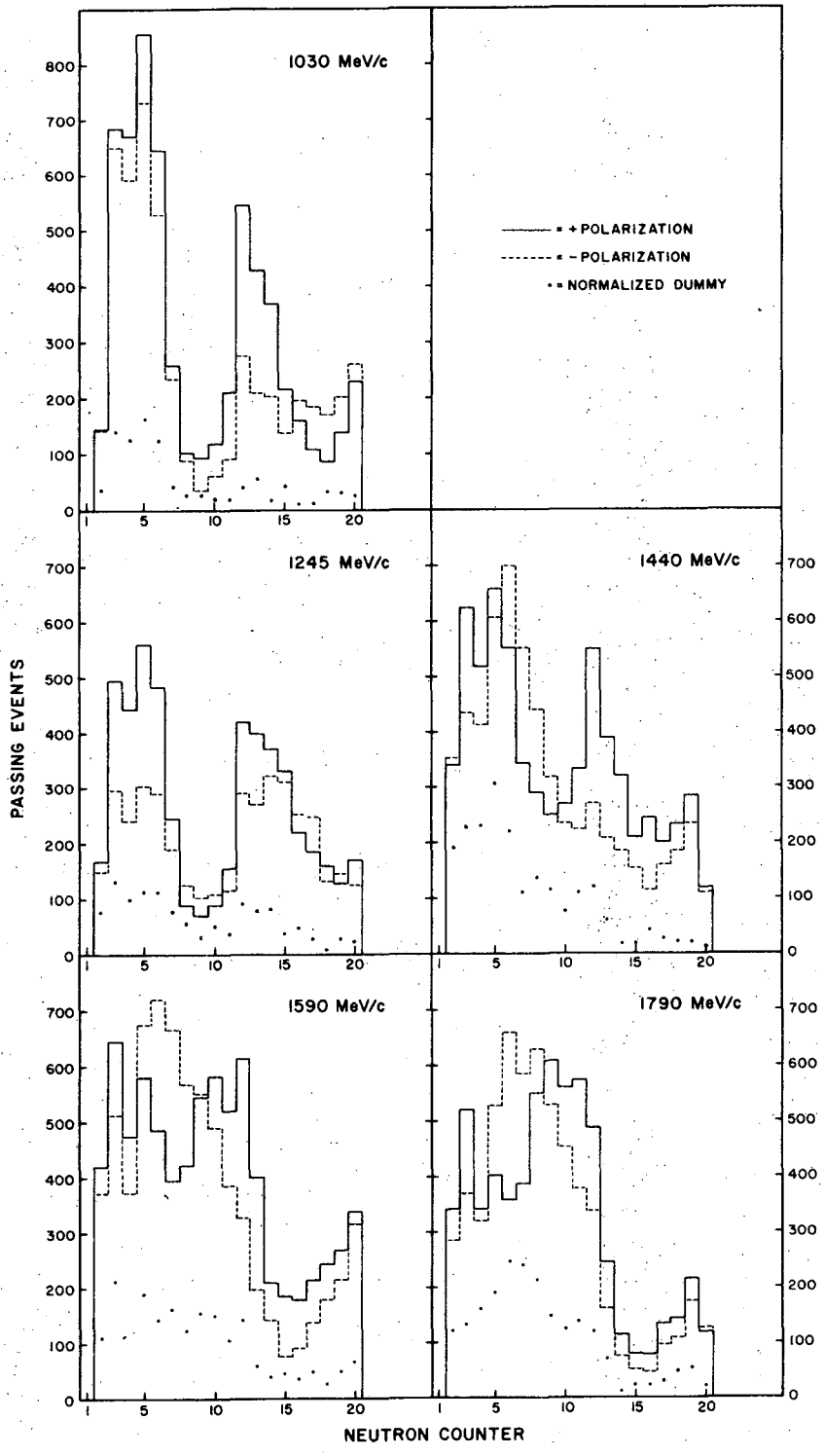

Fig. 14. For each momentum, the passing events are displayed for each sign of target polarization (+ means up, - means down; the direction of $\hat{n}$ is down). The estimated background is included.

V. RESULTS AND CONCLUSIONS

A. Results

Charge exchange polarization measurements have been made previously at higher energies,[22] primarily to test high energy interaction mechanisms, but with the exception of one very rough measurement by Hill et al.[23] at 310 MeV, this marks the first time that detailed measurements of $P(\theta)$ have been made in the region of energy where phase shift analyses are available (<2 GeV/c). However, measurements by the group at Rutherford are expected soon.

In Figs. 15 a-e the data from this experiment are compared with the predictions from the recent phase shift analyses of Saclay[24] and CERN.[25] Qualitatively, the data show general agreement with the predictions of both phase shift analyses at the lower momenta (except for the backward region of 1030 MeV/c), but show better agreement at the higher momenta with the Saclay 1973 phase shift predictions than with those of CERN. In particular, the disagreement with Almehed and Lovelace at 1790 MeV/c is quite severe. It should also be noted that the charge-exchange differential cross section data of Nelson, et al. show strong disagreement with Almehed and Lovelace at 1790 MeV/c (and also at higher energies). To quantitatively see the effect of these new data, the phase shift analyses must be rerun with these data included in their data set. Then it will be possible to observe the change, if any, in the individual phases and inelasticities. This program will be carried out at this laboratory using the programs of Kelly and Cutkosky,[26] and possibly

with updated programs of Johnson et al.[1]

There are two regions of disagreement between our data and the Saclay (1973) smoothed phase shifts. The first occurs in the backward region of 1030 MeV/c. Although there is some uncertainty in the background subtraction in this region, the polarization parameter is rather insensitive to this uncertainty because of the large number of events in the hydrogen peak in this region. The other disagreement occurs in the forward direction of 1790 MeV/c, where there is no indication for the oscillatory behavior predicted by Saclay. However, in this case, it should be pointed out that none of the data points is more than two standard deviations from the predicted values.

The isospin bounds shown on the figures are those reported by Ayed, et al.[24] using the Saclay (1973) smoothed phase shifts. The isospin bounds can be calculated from the triangular relations for the transversity cross-sections,[27] indicated below. A brief derivation of these relations follows. The expressions for the differential cross-sections and polarization parameter measurements in terms of the charge amplitudes are

$$I_o^+ = |f_+|^2 + |g_+|^2$$
$$I_o^- = |f_-|^2 + |g_-|^2$$
$$I_o^o = 1/2|f_+ - f_-|^2 + 1/2|g_+ - g_-|^2$$

$$(I_oP)^+ = -2Imf_+^*g_+$$
$$(I_oP)^- = -2Imf_-^*g_-$$
$$(I_oP)^o = -Im(f_+ - f_-)^*(g_+ - g_-)$$

The transversity amplitudes can be defined via the following transformations

$$F_R = \frac{1}{\sqrt{2}}(f_+ + ig_+) \qquad G_R = \frac{1}{\sqrt{2}}(f_- + ig_-)$$

$$F_L = \frac{1}{\sqrt{2}}(f_+ - ig_+) \qquad G_L = \frac{1}{\sqrt{2}}(f_- - ig_-)$$

In terms of these transversity amplitudes, the expressions for I_o^q and p^q become (the superscript q denotes the charge of the final pion)

$$I_o^+ = |F_R|^2 + |F_L|^2$$
$$(I_oP)^+ = |F_R|^2 - |F_L|^2$$

$$I_o^- = |G_R|^2 + |G_L|^2$$
$$(I_oP)^- = |G_R|^2 - |G_L|^2$$

$$I_o^o = 1/2(|F_R|^2 + |F_L|^2 + |G_R|^2 + |G_L|^2) - Re F_R{}^*G_R - Re F_L{}^*G_L$$
$$(I_oP)^o = 1/2(|F_R|^2 - |R_L|^2 + |G_R|^2 - |G_L|^2) - Re F_R{}^*G_R + Re F_L{}^*G_L$$

Defining the transverse cross-sections

$$I_\pm^q = I_0^q(1 \pm p^q)$$

the above equations for the differential cross-section and polarization parameter for the charge exchange reaction can be written:

$$2I_\pm^0 = I_\pm^+ + I_\pm^- - 2(I_\pm^+ I_\pm^-)^{1/2}\cos\delta_\pm$$

where $\delta_+(\delta_-)$ is the still undetermined relative phase between the transversity amplitudes F_R, G_R (F_L,G_L). The variation of $\cos\delta_\pm$ between ± 1 in the above equation gives the triangular relations for the transversity cross-sections.

It should be noted that almost all of the data points from this experiment lie within these bounds; the possible exception is the back-

ward region at 1245 MeV/c, but it should be pointed out that the Saclay predictions are for 1282 MeV/c, rather distant in energy from our data. However, 1245 MeV/c was the first momentum at which we took data and which was troubled by difficulties with the polarized target, resulting in a greater normalization error for the target polarization, and hence for the polarization parameter.

Real zeroes in the transversity amplitudes occur at the values $P(\theta) = \pm 1$. Analyses depending on knowledge of the zeroes in the amplitudes rely heavily on knowing the precise values of energy and angle where this relationship is true. For this reason, the values of $\cos\theta$ for which the measured polarization parameter is large (in $\pi^- p \to \pi^0 n$) are summarized below.

1030 MeV/c	$-.2<\cos\theta<.2$	and	$\cos\theta \sim .65$
1245 MeV/c	$\cos\theta \sim -.55$		
1440 MeV/c	$\cos\theta \sim .23$		
1590 MeV/c	$.50<\cos\theta<.60$	and	$\cos\theta \sim .26$; $\cos\theta \sim -.28$
1790 MeV/c	$\cos\theta \sim .35$		

Tests of possible systematic errors were made by checking for non-zero false asymmetries. For example, if the data were taken in runs having the sequence of target polarizations ++--++--++--..., a test of a possible false asymmetry can be made using in the analysis programs a sequence like +--++--++--+... where half of the positively (negatively) polarized data is misidentified as being negatively (positively) polarized. Two tests were made on these data: 1) every other event had the sign of target polarization opposite to its true value, and 2) the data were sequentially identified by run, and the

false asymmetry test was made as indicated above. The computed false asymmetries fit the hypothesis of zero asymmetry with the following confidence levels (for the second test)

1030 MeV/c -- 52%
1245 MeV/c -- 64%
1440 MeV/c -- 97%
1590 MeV/c -- 80%
1790 MeV/c -- 47%

The first test also gave false asymmetries closely consistent with zero.

The final results are given in Table VI. A discussion of the errors may be found in Appendix C. The errors quoted in the table are statistical only. A summary of the systematic errors in the polarization parameter are tabulated below. (A conservative factor of two has been applied to the calculation of the error in the target polarization.)[12a] The error in the monitor is an estimate of the disagreement between the "failing" events and the "interaction" monitor. This correction enters through the background subtraction.

Table V.

Source	Systematic Error Contribution				
	1030 MeV/c	1245 MeV/c	1440 MeV/c	1590 MeV/c	1790 MeV/c
Target Polarization	5%	8%	5%	5%	5%
False Asymmetry	0%	0%	0%	0%	0%
Overall Monitor	4%	5%	3%	3%	3%
Relative Systematic Error	(1±0.06)	(1±0.09)	(1±0.06)	(1±0.06)	(1±0.06)

Polarization parameter $P(\theta)$ in $\pi^- p \to \pi^\circ n$ scattering.

The error $\Delta P(\theta)$ is statistical only.

Table VI. a)

P_{lab} = 1.030 GeV/c	T_{lab} = 0.900 GeV		E_{cm} = 1688 GeV
Cos θ_{cm}	-t	P(θ)	ΔP(θ)
-.882	1.233	.26	.09
-.815	1.189	-.15	.17
-.741	1.141	-.11	.08
-.660	1.088	-.11	.07
-.572	1.030	-.24	.07
-.450	.950	-.22	.08
-.365	.894	-.14	.12
-.235	.809	-.26	.21
-.164	.763	-1.48	.65
-.099	.720	-.67	.18
-.014	.665	-.82	.15
.168	.545	-.77	.09
.256	.487	-.82	.11
.347	.428	-.56	.09
.464	.351	-.44	.12
.535	.305	.20	.13
.604	.260	.61	.15
.655	.226	.94	.23
.705	.193	.46	.15
.755	.161	.24	.10

Table VI. b)

P_{lab} = 1.245 GeV/c	T_{lab} = 1.113 GeV		E_{cm} = 1803 GeV
Cos θ_{cm}	-t	P(θ)	ΔP(θ)
-.802	1.513	-.42	.30
-.724	1.447	-.75	.19
-.639	1.376	-1.11	.18
-.547	1.299	-1.16	.17
-.420	1.192	-.93	.17
-.332	1.118	-.51	.21
-.200	1.007	.92	.84
-.128	.947	.26	.27
-.063	.892	.41	.47
.022	.821	-.88	.47
.203	.669	-.47	.12
.290	.596	-.58	.13
.379	.521	-.27	.12
.492	.426	-.18	.10
.561	.369	-.02	.12
.627	.313	.17	.11
.676	.272	-.36	.13
.723	.232	.02	.18
.770	.193	-.57	.16

Table VI. c)

P_{lab} = 1.440 GeV/c	T_{lab} = 1.307 GeV		E_{cm} = 1901 GeV
Cos θ_{cm}	-t	P(θ)	ΔP(θ)
-.866	1.884	.92	.28
-.791	1.808	-.10	.19
-.708	1.725	-.65	.23
-.620	1.636	-.53	.19
-.524	1.539	-.19	.12
-.394	1.407	.31	.11
-.304	1.317	.65	.15
-.170	1.181	.48	.14
-.097	1.108	.20	.14
-.031	1.041	-.17	.14
.054	.955	-.57	.19
.234	.774	-.97	.15
.319	.688	-.78	.15
.406	.600	-.52	.10
.516	.489	-.30	.10
.582	.422	-.72	.19
.645	.358	-.27	.12
.693	.310	-.24	.13
.738	.265	-.24	.08
.783	.219	-.09	.19

Table VI. d)

P_{lab} = 1.590 GeV/c	T_{lab} = 1.457 GeV		E_{cm} = 1973 GeV
Cos θ_{cm}	-t	P(θ)	ΔP(θ)
-.860	2.125	.20	.32
-.781	2.036	-.19	.12
-.697	1.938	-.33	.12
-.605	1.834	-.51	.22
-.507	1.722	.21	.10
-.374	1.570	.64	.12
-.283	1.465	.88	.15
-.146	1.310	.24	.12
-.074	1.227	-.02	.10
-.008	1.151	-.33	.13
.077	1.054	-.37	.10
.256	.850	-.87	.15
.340	.754	-.77	.11
.425	.657	-.56	.18
.533	.534	-1.16	.29
.598	.460	-.82	.18
.659	.390	-.63	.18
.705	.337	-.36	.13
.749	.287	-.24	.11
.792	.238	-.10	.10

Table VI. e)

P_{lab} = 1.790 GeV/c	T_{lab} = 1.656 GeV	E_{cm} = 2066 GeV	
$\cos\theta_{cm}$	-t	P(θ)	ΔP(θ)
-.770	2.338	-.38	.18
-.681	2.221	-.43	.13
-.586	2.096	-.33	.22
-.485	1.962	.40	.13
-.348	1.781	1.06	.29
-.255	1.658	.65	.21
-.117	1.476	.39	.12
-.044	1.380	-.15	.10
.022	1.292	-.23	.10
.107	1.180	-.61	.16
.283	.947	-.52	.11
.366	.838	-.79	.27
.449	.727	-.38	.17
.554	.590	-.26	.27
.616	.507	-.44	.38
.675	.429	-.38	.17
.719	.371	-.28	.16
.761	.315	-.27	.14
.803	.261	.08	.17

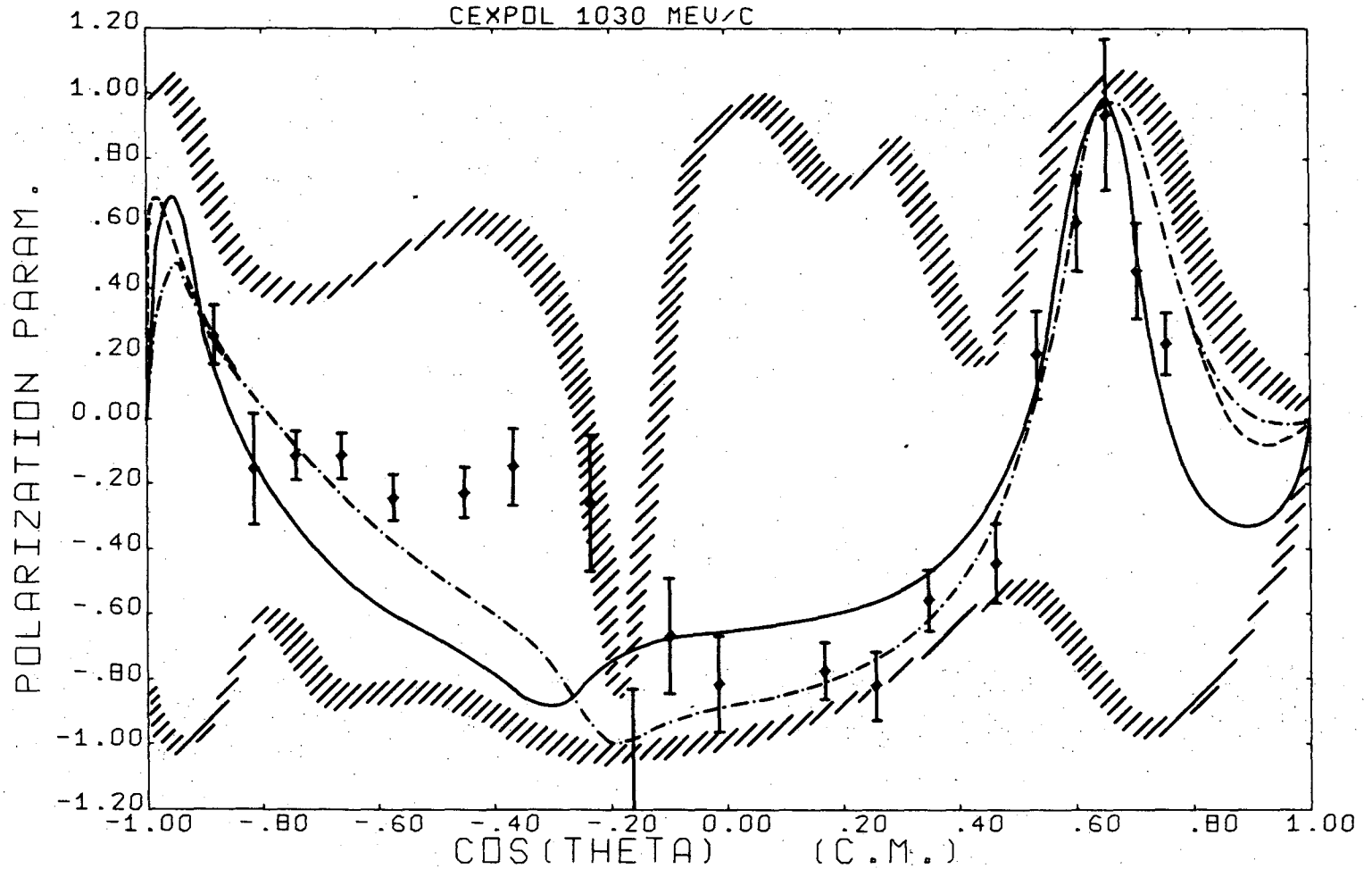

XBL 741-38

Fig. 15 a. Polarization parameter for the reaction $\pi^- p \rightarrow \pi^0 n$ as measured in this experiment; comparison is made with the phase-shift analyses predictions of Almehed et al. (——, 1030 MeV/c), Saclay (1973: ----, 1030 MeV/c), and Saclay (1972: -·-·-·-, 1030 MeV/c), none of which included the data presented here. The isospin bounds (///) were calculated from the Saclay (1973) phase shifts.

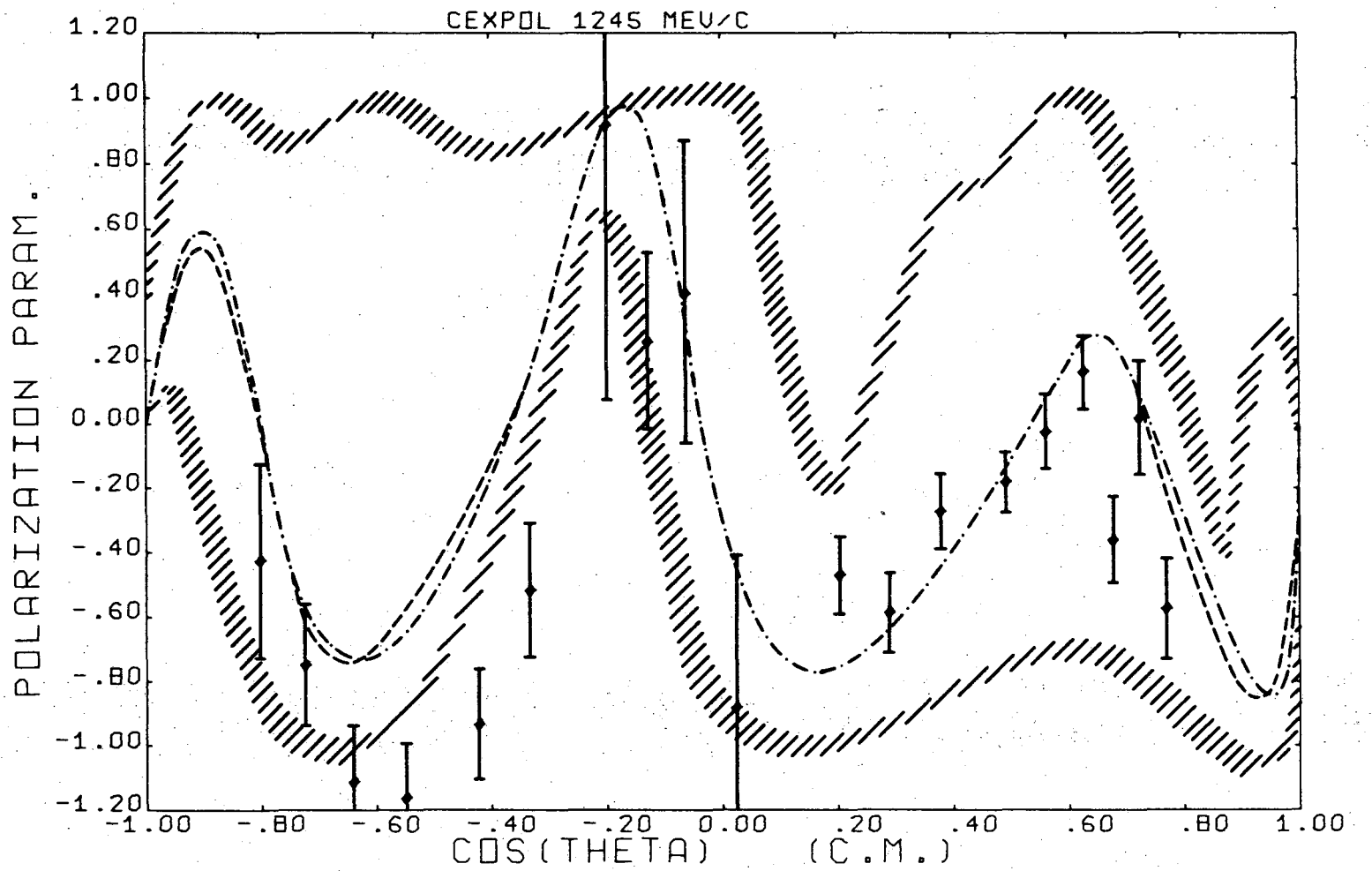

XBL 741-40

Fig. 15 b. Polarization parameter for the reaction $\pi^- p \to \pi^0 n$ as measured in this experiment; comparison is made with the phase-shift analyses predictions of Saclay (1973: ----, 1282 MeV/c), and Saclay (1972: -·-·-·-, 1282 MeV/c), neither of which included the data presented here. The isospin bounds (///) were calculated from the Saclay (1973) phase shifts.

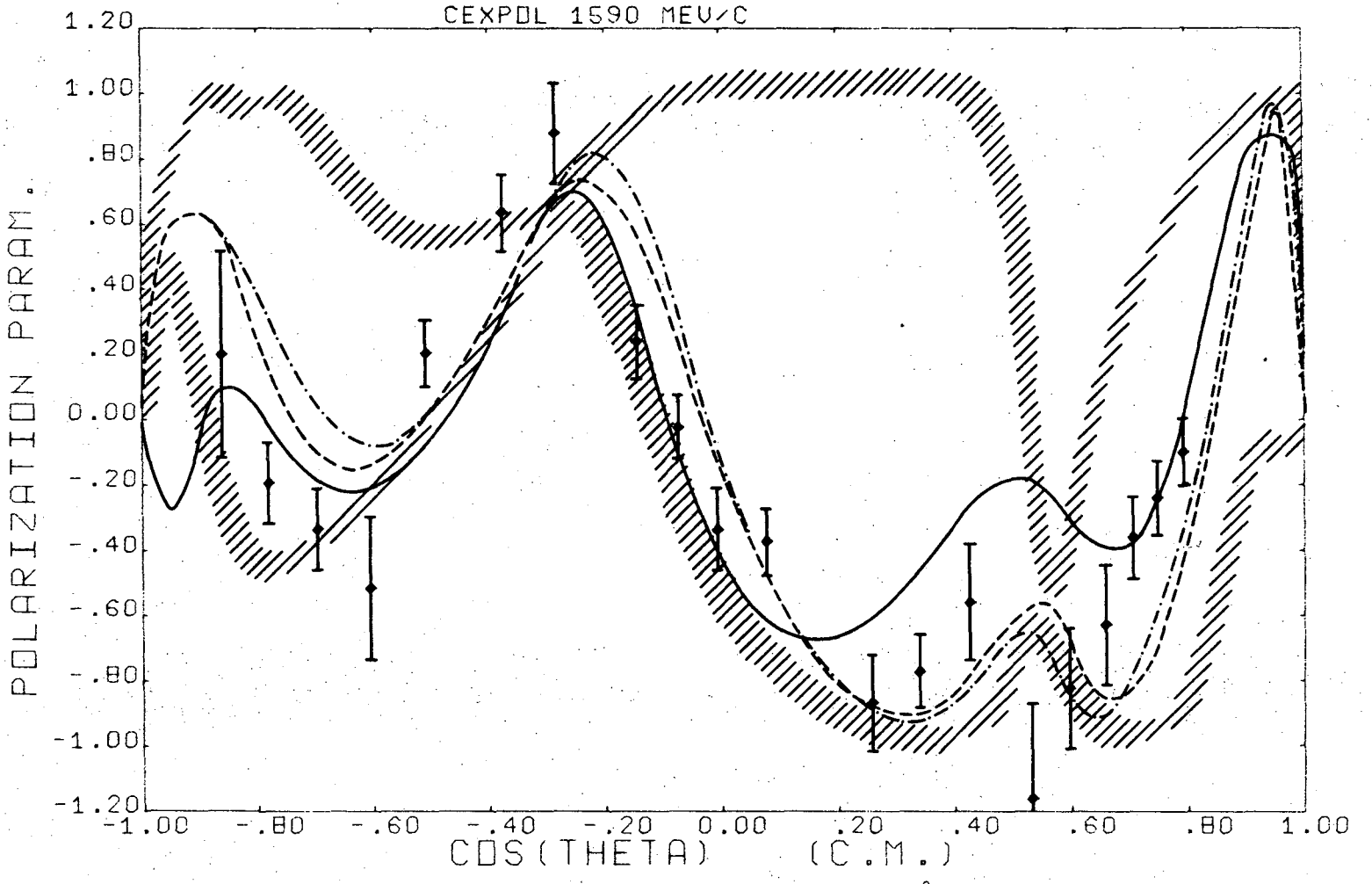

Fig. 15 c. Polarization parameter for the reaction $\pi^- p \to \pi^0 n$ as measured in this experiment; comparison is made with the phase-shift analyses predictions of Almehed et al. (——, 1579 MeV/c), Saclay (1973: ----, 1578 MeV/c), and Saclay (1972: ·-·-·-·, 1578 MeV/c), none of which included the data presented here. The isospin bounds (///) were calculated from the Saclay (1973) phase shifts.

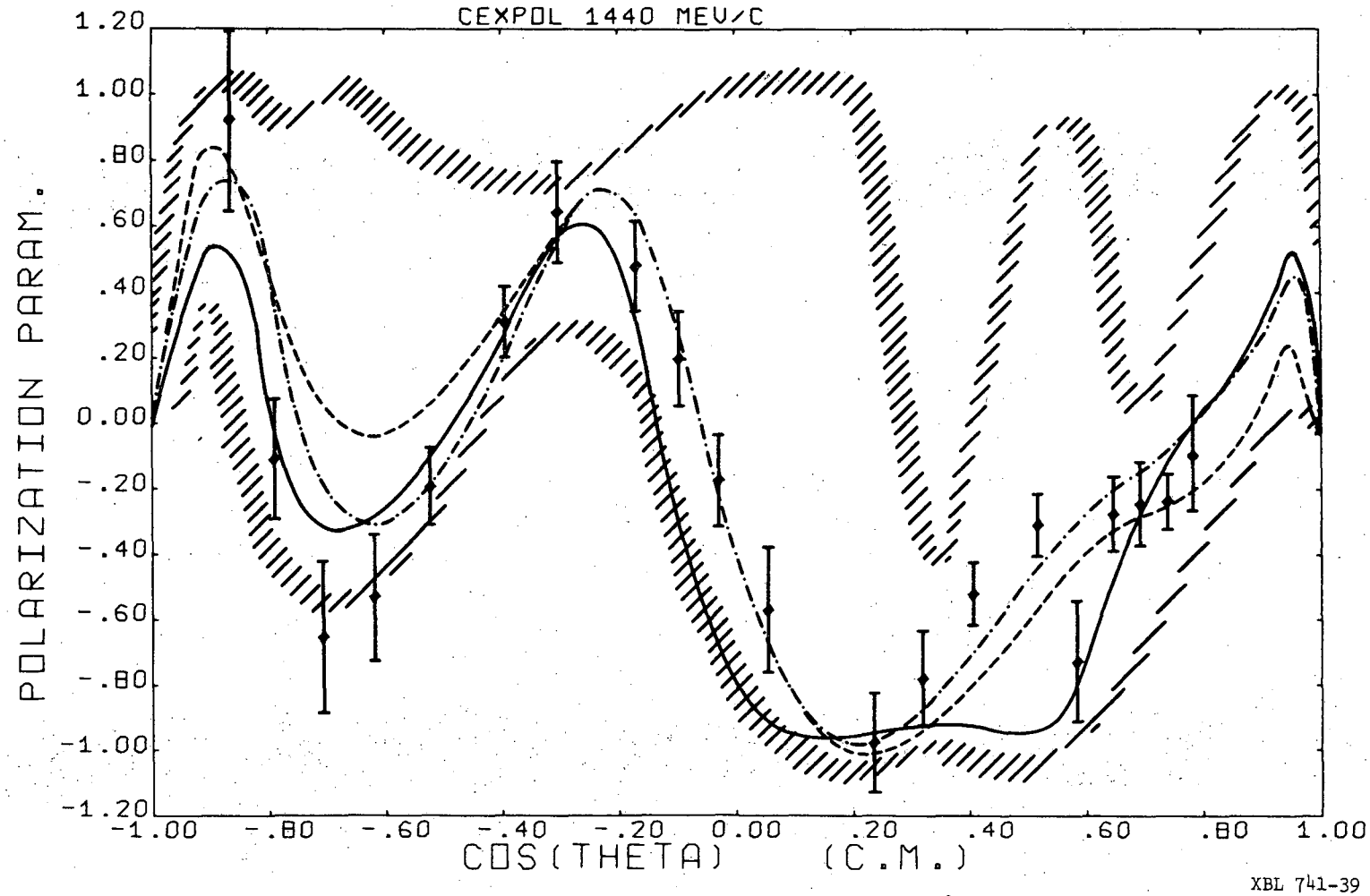

XBL 741-39

Fig. 15 d. Polarization parameter for the reaction $\pi^- p \to \pi^0 n$ as measured in this experiment; comparison is made with the phase-shift analyses predictions of Almehed it al. (——, 1441 MeV/c), Saclay (1973: ----, 1438 MeV/c), and Saclay (1972: -·-·-·-, 1438 MeV/c), none of which included the data presented here. The isospin bounds (///) were calculated from the Saclay (1973) phase shifts.

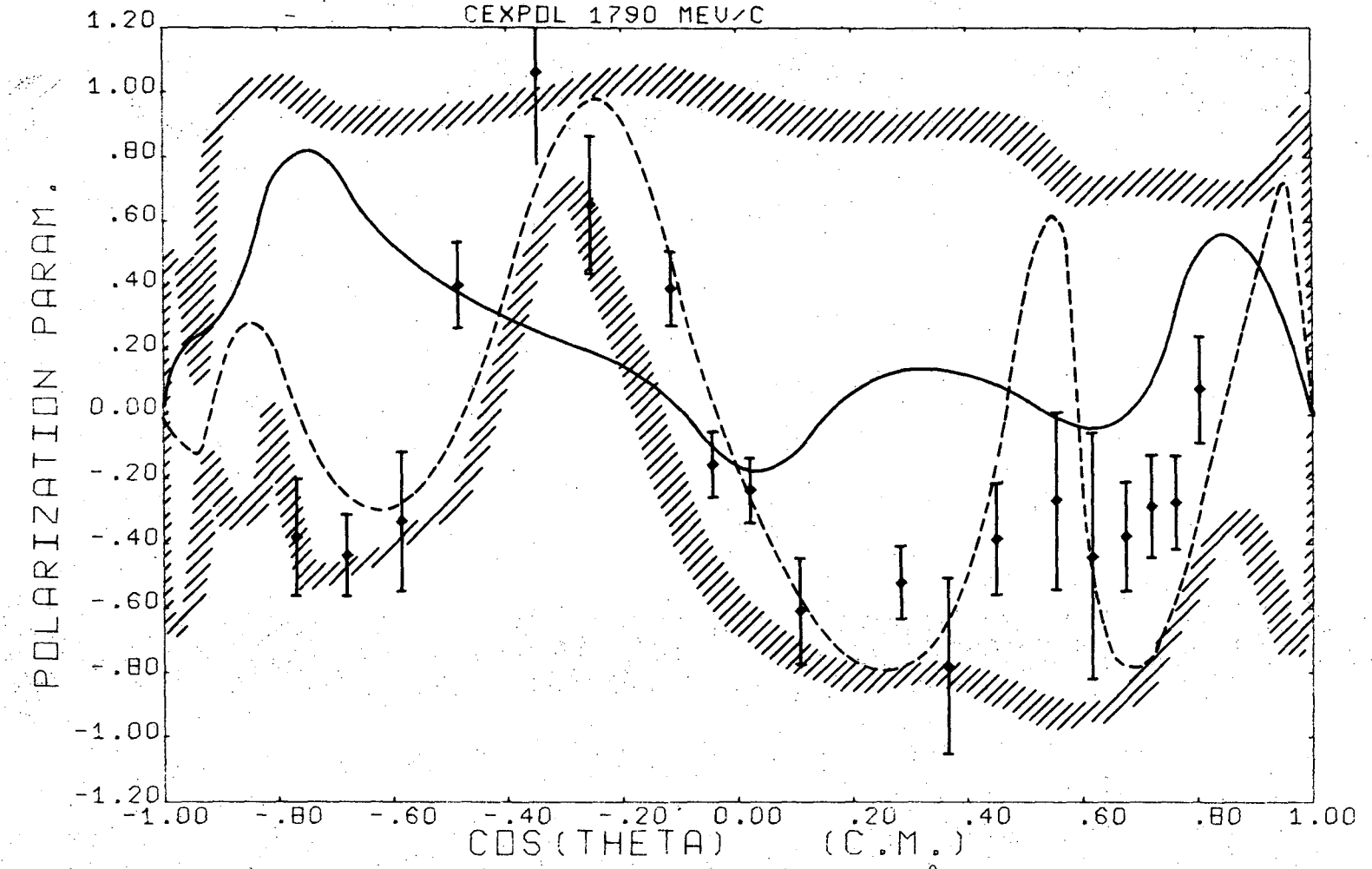

Fig. 15 e. Polarization parameter for the reaction $\pi^- p \to \pi^0 n$ as measured in this experiment; comparison is made with the phase-shift analyses predictions of Almehed et al. (——, 1801 MeV/c), and Saclay (1973: -·-·-·-, 1737 MeV/c), neither of which included the data presented here. The isospin bounds (///) were calculated from he Saclay (1973) phase shifts.

B. Conclusions

This experiment was performed with the hope that it would lead to a definitive set of phase shifts which would agree with known data, and have some predictive power for reactions not yet measured. The next step is to incorporate the data from this experiment into the phase shift analyses, and hopefully constrain the solutions to a unique set. If there are still several solutions, measurements of A and R parameters (or some appropriate linear combination of them) are necessary in order to provide further constraints. (As noted by Dean and Lee,[2] measurements of either $A^+(\theta)$ and $R^-(\theta)$, or $A^-(\theta)$ and $R^+(\theta)$ will enable explicit evaluation of the pion-nucleon amplitudes without using phase-shift analyses. Once we have obtained the pion-nucleon amplitudes in this low-energy region, what physics will they affect? Foremost is the clarification of the resonant particle spectrum, and the hope that it will give insight as a low energy model for the "strange" resonances as well. Together, these can shed light on the underlying group structure ($SU_{(3)}$, $SU_{(6)}$, or other models). In addition, a check can be made of forward and non-forward dispersion relations, and one can possibly hope to calculate high-energy Regge parameters for pion-nucleon interactions using the ideas of duality and finite energy sum rules.

A measurement of the polarization parameter in the charge-exchange reaction at high energies is a sensitive test of the various models of high energy interaction mechanisms (for example, the simple Regge prediction of zero polarization, providing only ρ-exchange contributes). My interest has been heightened by the possibility of making this measurement at the National Accelerator Laboratory, hopefully taking advantage of the experience gained from this experiment.

REFERENCES

1. C. H. Johnson, Measurement of the Polarization Parameter in $\pi^+ p$ Scattering from 750 to 3750 MeV/c (Ph.D. thesis), UCRL-17683 (unpublished).
2. N. W. Dean and Ping Lee, Phys. Rev. 5, No. 11, 2741 (1972).
3. R. L. Kelly, J. C. Sandusky, and R. E. Cutkosky, Carnegie Mellon Univ. #COO-3066-33 (submitted for publication).
4. E. Barrelet, Nuovo Cimento 8A, 331 (1972).
5. A. Gersten, Nuc. Phys. B12, 537 (1969).
6. J. E. Nelson, R. B. Chaffee, O. I. Dahl, R. W. Kenney, I. R. Linscott, M. Pripstein, T. B. Risser, A. Skuja and M. A. Wahlig, Physics Letters 47B, No. 281 (1973).
7. T. J. Devlin, OPTIK: An IBM-709 Computer Program for the Optics of High Energy Particle Beams, UCRL-9727 (1961), and R. Chaffee (private communication).
8. A. C. Paul, UCID-3416 (1970).
9. R. Chaffee, private communication.
10. G. Shapiro, private communication.
11. J. Jaros, private communication.
12. a) C. C. Morehouse, Photoproduction of π^+ Mesons from a Polarized Proton Target at 5 and 16 GeV (Ph.D. Thesis), UCRL-19897 (unpublished), p. 65.
    b) G. Shapiro in Progr. in Nucl. Techn. and Instrumentation, Vol. I, p. 173 (North Holland Publishing Co., Amsterdam, 1964).
    c) M. Borghini, Ecole Internationale de la Physique des Particules Elementaires, Herceg Novi, Yugoslavia (1968).
13. C. D. Jeffries, Dynamic Nuclear Orientation (Interscience Publishers, Inc., New York, 1963).

14. Q. A. Kerns, H. W. Miller and A. H. Wolverton, Chamberlain Proton Spin Resonance RF System 1260, UCRL-17548, Vol. I., Vol. II (unpublished).

15. T. B. Risser, "Neutral Decays of the η° Meson" (Ph.D. Thesis) UCRL-20039 (1970) (unpublished).

16. a) R. J. Cence, B. D. Jones, V. Z. Peterson, V. J. Stenger, J. Wilson, D. Cheng, R. D. Eandi, R. W. Kenney, I. Linscott, W. P. Oliver, S. Parker, and C. Rey, Phys. Rev. Letters 22, 1210 (1969).
b) C. A. Rey and S. I. Parker, Nuc. Instr. Meth. 54, 314 (1967); 43, 361 (1966).

17. A. R. Clark, L. T. Kerth, Proc. 1966 Inter. Conf. on Instrumentation for High Energy Physics, Stanford, California (1966), p. 355.

18. M. Leavitt, LBL Group A programming note p-188 (unpublished).

19. I. Linscott, M. Leavitt, O. Dahl, and A. Skuja (private communication).

20. C. O. Gimber, M. Leavitt and R. Chaffee, LBL Group A programming note p-194 (unpublished).

21. O. I. Dahl, T. B. Day, F. T. Solmitz and N. L. Gould, Group A programming note p-126 (unpublished).

22. a) P. Bonamy, et al., Nucl. Phys. B16, 335 (1970). (Saclay-Orsay-Pisa group at 5.1 and 11.2 GeV/c).
b) P. Bonamy, et al., Nucl. Phys.B52, 392 (1973). (Saclay-DESY group at 5 and 8 GeV/c).
c) D. D. Drobnis, et al., Phys. Rev. Letters 20, 274 (1968). (Argonne at 3.47 and 5. GeV/c).
d) D. Hill, et al., Phys. Rev. Letters 30, 239 (1973). (ANL-NAL-Northwestern-Maryland group at 3.5 and 5.0 GeV/c).

23. R. E. Hill, et al., Phys. Rev. D2, 1199 (1970), (LRL group, one point at T=310 MeV)

24. a) R. Ayed, et al., Phys. Letters 31B, No. 9, 598 (1970).
b) Saclay (1973) smoothed phase shifts, P. Bareyre, private communication, and R. Ayed, et al., Paper No. 311 presented at the Second International Conference on Elementary Particles, Aix-en-Provence, France (1973).

25. S. Almehed and C. Lovelace, Nucl. Phys. B40, 157 (1972).

26. R. Kelly, private communication.

27. G. Hohler, F. Kaiser, H. Kohl, and W. Schmidt, Nuovo Cimento Letters 5, 415 (1972).

28. R. J. Kurz, UCRL-11339.

29. P. R. Robrish, Backward Neutron-Proton Scattering with a Polarized Target (Ph.D. Thesis), LBL-1334 (unpublished).

30. P. D. Grannis, Measurement of the Polarization Parameter in Proton-Proton Scattering from 1.7 to 6.1 GeV (Ph.D. Thesis), UCRL-16070, pp. 99-101.

APPENDIX A.

Calibration and Maintenance of Threshold

The calibration and maintenance of the neutron counters required a detailed procedure to achieve optimum efficiency, minimum time slewing, and have constant gain throughout the experiment.

The program TOTEFF[28] calculated the neutron detection efficiency as a function of incident neutron kinetic energy for a series of input thresholds, as shown in Fig. 16. From these, we were able to derive the expected pulse height distributions (Fig. 17) for counters N_{10}-N_{20}, which had charge-exchanged neutrons of incident kinetic energy less than 400 MeV. The distributions shown are those expected for incident beam momentum 1030 MeV/c. Actually, the distributions were probability distributions for certain amounts of energy deposited in the counter for a given incident neutron energy, but in the linear operating region of the photomultiplier tube, the distributions are directly related. The TOTEFF calculations have been experimentally checked only up to 125 MeV (and are valid to within the claimed accuracy of ±10%), but since the program presently includes neutron cross-section data to 400 MeV, we relied on its predictions up to that energy.

The optimum high voltages of the neutron counters were determined by the use of two overlapping procedures, one for counters N_1-N_{10}, and the other for counters N_{10}-N_{20}.

The procedure for each of these counters N_i was to interpolate from Fig. 16 that energy E_i (equivalent electron energy) such that 90% of all charge-exchange events detected in that counter deposited energy $E>E_i$.

From the quantity E_i an attenuation value which set the threshold higher than 2.37 MeV equivalent electron energy was calculated, and the high voltage set in the following way.

The observation of the energy spectrum of the recoil electrons from the Compton scattering of 2.62 MeV gamma rays provided us with the afore-mentioned calibration energy, namely the sharp cutoff in the spectrum at $T_{e^-}^{max} = 2.37$ MeV, which is known as the "Compton edge". These gamma rays came from an excited state of Pb^{208}, the end product of a sequence of α and β decays beginning with the parent nucleus Th^{228}. Accordingly, the radioactive source was placed near the neutron counter, with the gamma rays scattering at random throughout the counter. With the circuit shown below, the energy spectrum was analyzed and displayed on the PHA. The variable attenuator was adjusted so that the half-height point of the experimental Compton edge fell on some particular, but arbitrarily chosen, PHA channel. With the radioactive source then removed, a light pulser is placed on the neutron counter N_i, and the pulser adjusted so that it gives an amount of energy E_i into the counter.

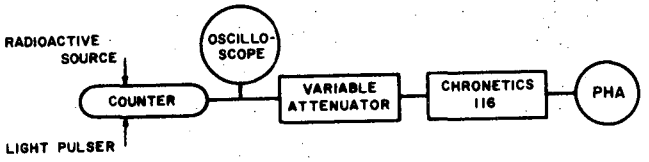

This was done by attenuating the input to the Chronetics 116 Linear Gate and Stretcher by a factor $E_i/2.37$ and adjusting the light pulser until the signal was centered on the PHA channel remarked above. Thus, with the attenuation removed from the input to the Chronetics 116,

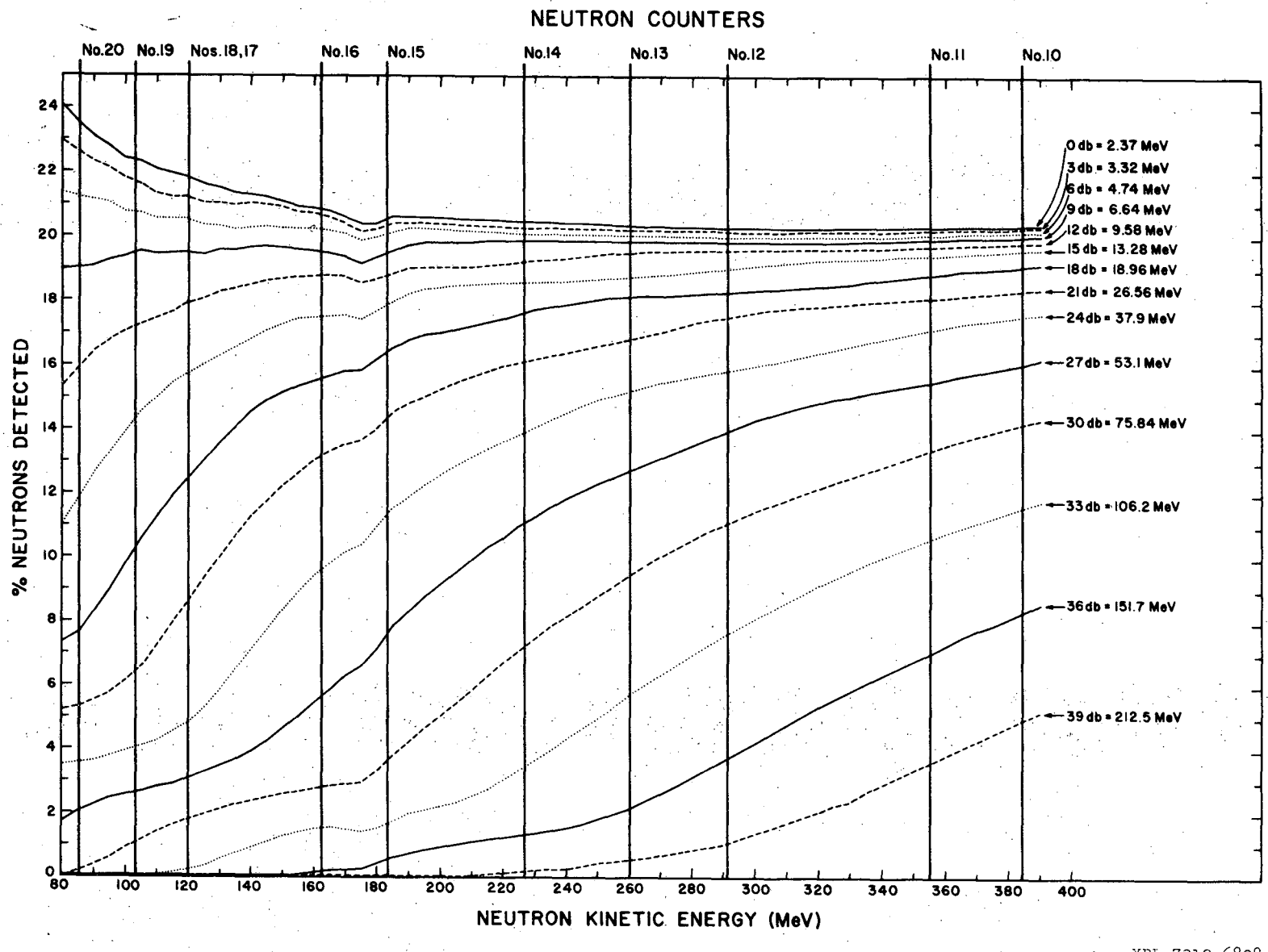

XBL 7312-6828

Fig. 16. Neutron detection efficiency as a function of neutron kinetic energy.

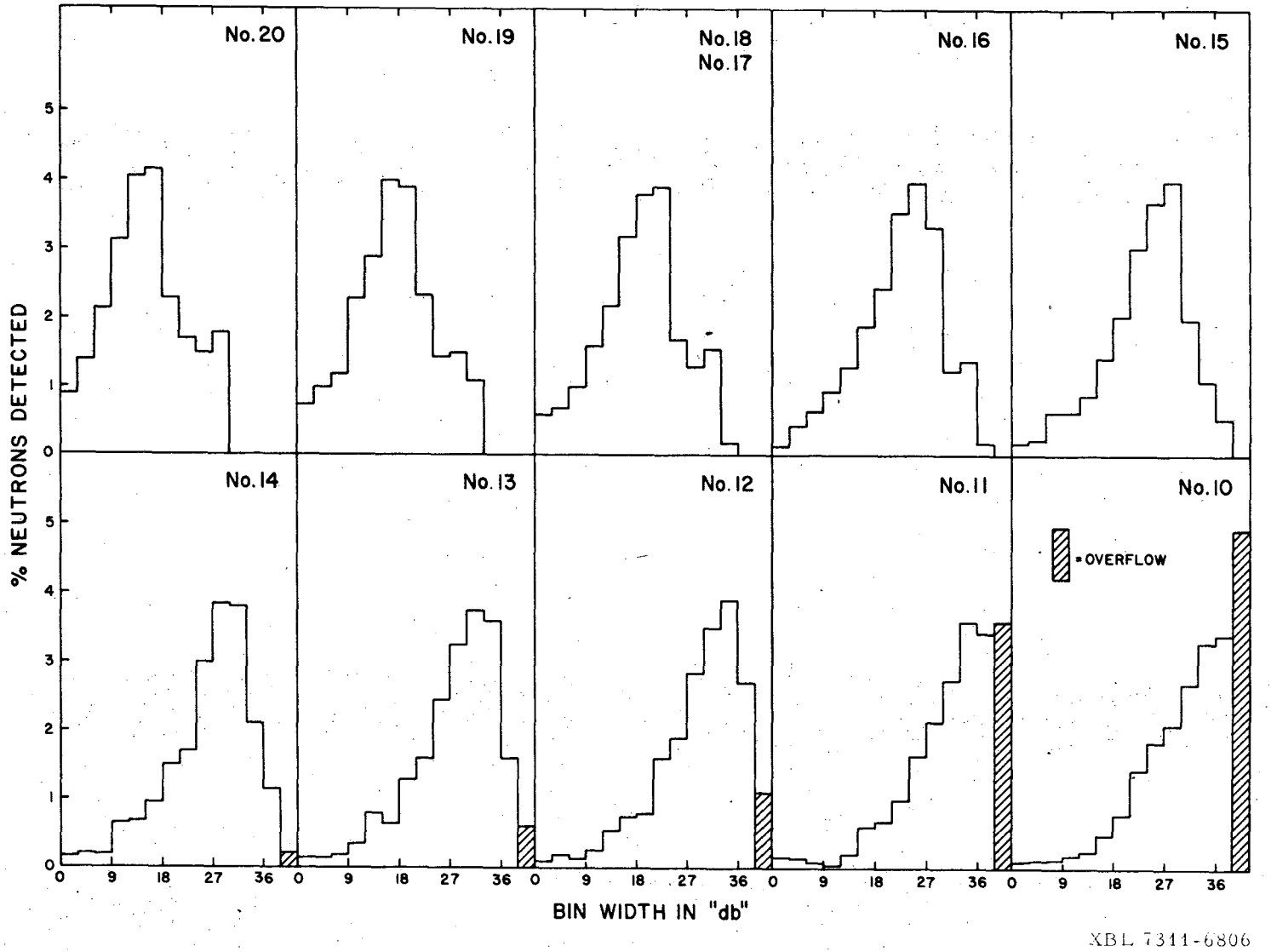

XBL 7311-6806

Fig. 17. Expected pulse height distributions in neutron counters 10-20 for 1030 MeV/c.

an equivalent electron energy of E_i was deposited in the counter. The high voltage was then set to give an anode pulse height of 1 volt. This pulse height was chosen as a result of tests of time slewing versus pulse height. Pulse heights less than ∿1 volt were found to slew badly; the timing circuitry required the bipolar pulse to have a steep slope as it changed polarity, and the small pulse heights did not satisfy that criterion. With the circuit restored to its original configuration, and the radioactive source used once again, the Compton edge was shifted to a new PHA channel, since the high voltage of the counter had been changed.

The procedure for the other counters N_1-N_9 made use of this knowledge of the Compton edge for N_{10}. The half-height of the Compton edge for each of the counters N_1-N_9 was set at the same PHA channel as was found for counter N_{10}, by varying the high voltage of each of them in turn. Once the voltages had been set, the discriminator output was used to gate the pulse height analyzer, and the threshold of the discriminator changed until the energy spectrum was cut off at the Compton edge.

At the moment when the threshold was set, a high intensity Th^{228} source (the 'GIANT' source) was exposed and pulses above threshold were counted for a specified time interval. The threshold of each counter was set separately and the counting rate with this standard source recorded.

When the attenuation was used to set the threshold higher than the 2.37 MeV equivalent electron energy, the calibration with the standard source was done with the attenuation removed. Calibration

of the discriminators was carried out once a week, when the Bevatron was off. For those thresholds which needed adjusting to achieve the correct count, it was considered preferable to change the discriminator threshold to match the change in gain rather than change the photomultiplier high voltage (changes in the photomultiplier high voltage substantially increase the gain fluctuations for several days), thus the high voltages on the tubes were held constant throughout the experiment.

The threshold discriminators were monitored by an automated digital system. This device sent input pulses to all 20 discriminators simultaneously. These input pulses were applied via ferrite cores to the signal cables from the phototubes. The cores were permanently in place and did not disturb the photomultiplier signals. A fast output from one discriminator at a time was sampled by the system. The input pulses were rapidly increased in size until the discriminator threshold was reached and an output pulse returned to the monitoring system. The threshold was then displayed digitally. The monitoring system was used to set, change, and observe the 20 discriminator thresholds.

APPENDIX B.

Calculation of the Polarization Parameter

A complete derivation of the formula used to compute the polarization parameter may be found elsewhere.[29] The basic ideas of the least squares fitting procedure follow.

The data are a set of measurements N_i, M_i and P_i which are respectively the number of events in the i^{th} run, the number of monitors in the i^{th} run, and the polarization of the target in the i^{th} run.

Writing $(\vec{P}_T \cdot \hat{n})_i = P_i$, equation (1) may be written for the i^{th} run as:

$$I_i(\theta) = I_o(\theta)\ [1 + P(\theta)P_i]\ .$$

In a plot of $I_i(\theta)$ versus $P_i(\theta)$, this equation represents a straight line of intercept $I_o(\theta)$ and slope $I_o(\theta)P(\theta)$. $I_i(\theta)$ is the number of elastic scattering events per unit monitor in the hydrogen peak corresponding to the center-of-mass angle. It is obtained from the total number of events (N_i) in the hydrogen peak of the polarized target data, and the number of background counts (B_i) determined from the dummy data. B_i can be calculated from the ratio of the number of monitor counts for the polarized target (M_i) and the dummy target (C), and the total number of dummy counts (D) in the equivalent region to the hydrogen peak, namely $B_i = \frac{M_i}{C} D$.

However, a more accurate method of estimating the background was used in this analysis, which matched the spectra of non-hydrogen events from the polarized target and the dummy target, and then computed the correct normalization ratio. Thus, we can write for a given center of

momentum angle:

$$H_i = N_i - B_i = M_i I_o (1+PP_i)$$

where H_i is the number of hydrogen events in the elastic scattering peak.

We wish to find a value for P such that the function $f(I_o,P) = M_i I_o(1+PP_i)$ best represents H_i, for each center-of-momentum angle. In order to do this, we perform a least squares fit, in which we minimize the quantity

$$S = \sum_i \frac{[H_i - M_i I_o(1+PP_i)]^2}{\sigma_i^2}$$

where σ_i^2 is the mean square error of the i^{th} measurement of H_i. If H_i were large enough, we would assume a Gaussian distribution, giving a mean square error of H. However, H is generally small enough so that Poisson statistics are required. For a Poisson distribution, σ_i^2 is just the expected value of H_i; however, this is not known until we have found the minimizing parameters $\bar{I}_o$ and $\bar{P}$. Then $\sigma_i^2 = M_i \bar{I}_o(1+\bar{P}P_i)$ where σ_i^2 is not a function of I_o and P, but only of $\bar{I}_o$ and $\bar{P}$. Hence, since we first must find $\bar{I}_o$ and $\bar{P}$, the minimization requires an iterative solution.

Defining $I_i = I_o P$, the minimizing conditions are:

$$\frac{\partial S}{\partial I_o} = 0 \qquad \frac{\partial S}{\partial I_1} = 0$$

Straightforward calculation yields the result:

$$P = \frac{\sum_i \frac{M_i H_i P_i}{\sigma_i^2} - \langle p \rangle \sum_i \frac{M_i H_i}{\sigma_i^2}}{\langle p^2 \rangle \sum \frac{M_i H_i}{\sigma_i^2} - \langle p \rangle \sum \frac{M_i H_i P_i}{\sigma_i^2}}$$

where $\langle p^n \rangle$ equals

$$\frac{\sum_i \frac{M_i^2 p_i^n}{\sigma_i^2}}{\sum_i \frac{M_i^2}{\sigma_i^2}}$$

Using $\sigma_i^2 = M_i \bar{I}_o$ as the first choice in the iteration procedure, we obtain the zeroth order solution:

$$P^o = \frac{\sum_i H_i P_i - \langle p \rangle_o \sum_i H_i}{\langle p^2 \rangle_o \sum_i H_i - \langle p \rangle_o \sum_i H_i P_i}$$

where $\langle p^n \rangle_o$ equals

$$\frac{\sum_i M_i P_i^n}{\sum_i M_i} .$$

This solution has been found to be a quite accurate approximation if the magnitude of the target polarization is nearly constant throughout the running of the experiment, as it was for this experiment. This is the expression in general use for calculation of the polarization parameter, but it is not exact.

Rewriting the expressions to show explicitly the measured quantities N_i, M_i, P_i and the estimated background B_i we have (dropping the "zeroth order" notation)

$$P = \frac{\sum_i [(N_i-B_i)P_i] - \langle p\rangle \sum_i (N_i-B_i)}{\langle p^2\rangle \sum_i (N_i-B_i) - \langle p\rangle \sum_i [(N_i-B_i)P_i]} \tag{B1}$$

Defining the new variable $Q_i = P_i - \langle p\rangle$ which has the property that

$$\langle Q^2\rangle = \langle p^2\rangle - \langle p\rangle^2$$

we find

$$P = \frac{\sum_i [(N_i-B_i)Q_i]}{\langle Q^2\rangle \sum_i (N_i-B_i) - \langle p\rangle \sum_i [(N_i-B_i)Q_i]}$$

This can be rewritten in terms of a new parameter ϵ as

$$p = \frac{\epsilon}{1 - \epsilon\langle p\rangle} \tag{B2}$$

where ϵ is defined as

$$\epsilon = \frac{\sum_i [(N_i-B_i)Q_i]}{\langle Q^2\rangle \sum (N_i-B_i)}$$

Since the number of failing events is proportional to the number of monitors, i.e., $B_i = bM_i$, a proposition which has carefully checked for each of the momenta, and which was true within statistical error,

and since $\sum_i B_i = R\sum_j D_j$, the latter formula can be rewritten in the following way:

$$\varepsilon = \frac{\sum_i N_i Q_i}{\langle Q^2 \rangle \left(\sum_i N_i - R\sum_j D_j\right)} \tag{B3}$$

where R is the ratio of "failing" events from the polarized target data to the dummy target events.

APPENDIX C

Errors

1. Counting Errors and the Polarization Parameter

Counting statistics and the uncertainties associated with the measurement of the target polarization were the principal contributions to the error in the polarization parameter. The number of counts in the hydrogen peak determined the dominant error contribution. The number of monitor counts and the number of counts in the dummy target data used in the background subtraction added to the error. Another contribution to the error was from the normalization ratio determined by the failing polarized target events and the dummy events.

The number of interactions in the target was used as a monitor. This number was proportional to the number of failing events; the failing event/interact ratio for both signs of polarization agreed to within statistical error (2%). See the discussion on the event defining electronics for the definition of the 'interact' monitor.

The error in the polarization parameter is calculated from the expression

$$P = \frac{\varepsilon}{1 - \varepsilon\langle p\rangle}$$

giving

$$\delta P = [(\partial P/\partial \varepsilon)^2 \cdot (\delta\varepsilon)^2 + (\partial P/\partial\langle p\rangle)^2 \cdot (\partial\langle p\rangle)^2 + 2(\partial P/\partial\varepsilon)\cdot(\partial P/\partial\langle p\rangle)\cdot\delta\varepsilon\cdot\delta\langle p\rangle]^{1/2}$$

To a very good approximation, the last two terms give negligible contribution. Thus, with

$$(\partial P/\partial \varepsilon) = (1 - \varepsilon\langle p\rangle)^{-2}$$

we obtain

$$P = \left(\frac{1}{1-\varepsilon\langle p\rangle}\right)^2 \cdot \delta\varepsilon$$

where

$$\delta\varepsilon = \sum_i (\partial\varepsilon/\partial N_i)^2 \cdot (\delta N_i)^2 + \sum_i (\partial\varepsilon/\partial M_i)^2 \cdot (\delta M_i)^2 + \sum_i (\partial\varepsilon/\partial p_i)^2 \cdot (\delta p_i)^2 +$$

$$+ (\partial\varepsilon/\partial R)^2 \cdot (\delta R)^2 + (\partial\varepsilon/\partial(\sum_j D_j))^2 \cdot (\delta(\sum_j D_j))^2]^{1/2}$$

Partial differentiation of equation (B3) yields expressions for each of these terms; these may be found elsewhere.[30]

2. Other Sources of Error

During data taking, the sign of the target polarization was usually reversed approximately every two hours to minimize the error introduced by slow drifting of experimental conditions. The higher the frequency of such target reversals, the more such systematic errors cancel out. However, since the time to change the polarization of the target from one sign to the other was ∿10 minutes, in order to have reasonable continuity in the data taking, the reversal time was chosen accordingly.

Sources of error in the target polarization, scattering angle, and beam momentum are discussed below.

A. Target Polarization

Errors in the target polarization which scale the magnitude of the polarization up or down, rather than shift the zero of the polarization, can be related to the error in the polarization parameter according to

$$\frac{\Delta P(\theta)}{P(\theta)} = \frac{\Delta P_T}{P_T}$$

1) Errors in the target polarization measurement were obtainable from histograms which displayed the distribution of events as a function of target polarization for each run. When the target was operating stably, and that was the usual condition, $\frac{\Delta P_T}{P_T} \leq 0.5\%$

2) Calibration measurements of the polarization where the target was at thermal equilibrium (TE) were less precise, since here the target polarization was only about 0.18-0.20%. Typically, the TE calibration measurement was an average of twenty readouts, each readout being the result of eight sweeps through the resonance line in order to enhance the signal-to-noise ratio. The signals in Fig. 18 consist of the result of the eight sweeps for both the TE and background measurements. The typical rms deviation for the TE's was +/-3%, giving an uncertainty (with the target polarization $\sim$50%) of $\sim$0.8% in the target polarization. The enhancement of the polarized signal to the TE signal was $\sim$250. This error, although statistical in origin, gives a systematic error in the target polarization, and hence in the polarization parameter.

3) In calculating the value of the polarization from readouts of the (enhanced) polarized target during data taking, an average of the TE calibration factors measured before and

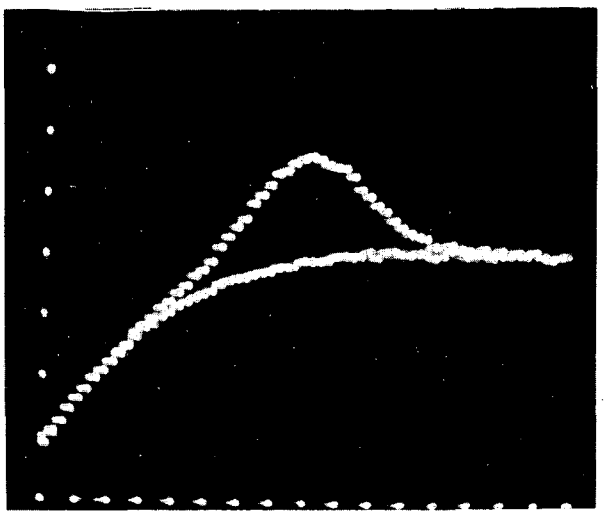

Fig. 18. Normal (eight-sweep) Thermal Equilibrium Signal with Background Superposed.

XBB 741-255

after the data taking period was used. These calibrations were generally taken twice a week; as a result, there were not enough data to provide a basis for Gaussian statistics. Except for a few instances where there was a large change in the calibration factor (which was explainable in terms of a significant change in the measurement system), these factors were consistent with statistical fluctuations. This error was characterized by $\Delta P_T/P_T$ generally lower than 3%. Since the average of two readings was used, this gave a systematic error of less than 1.5% for the typical target polarizations in this experiment.

4) Another source of systematic error was a change in the rf voltage driving the rf magnetic field in the cavity. This was monitored carefully for all the momenta (except 1245 MeV/c -- during half of that run there may have been a systematic error from this source of $\sim$7%). When these changes did occur, the rf level was restored and the data corrected later. The remaining error was difficult to estimate, but should have been less than 1% in the target polarization.

5) There also occurred shifts in the background subtracted from the total signal to give the resonance line. This error, unlike the previous ones, only shifts the zero of the target polarization. This shift was measured frequently during the data taking, and the target polarization corrected

accordingly. Residual error from this source was estimated to be $\Delta P_T/P_t \leq 0.3\%$. The resulting change in the polarization parameter for this kind of systematic error was the rather small error

$$\frac{\Delta P(\theta)}{P(\theta)} = (0.003) \cdot P(\theta)$$

B. Scattering Angle

The principal contributions to error in the scattering angle follow.

1) Uncertainty as to the position of the interaction point of the neutron within the neutron counter. The counters were 20.3 cm. in diameter, and with the distance from the center of the target to the center of the counter ranging from 375 - 500 cm., the angular uncertainty was 1 - 1.5°.

2) Uncertainty in the beam direction associated with the convergence of the beam typically was 1.5 - 2°. Hodoscope information was available on the beam direction, but was not used.

3) Uncertainty in the direction of the central ray of the beam at the point of interaction in the target due to the bending of the beam in the magnetic field of Zoltan ranged from $\pm$0.7° at 1790 MeV/c to $\pm$1.2° at 1030 MeV/c.

4) Uncertainty in the position of interaction in the target contributed an angular error of 0.4° - 0.6°.

5) Uncertainty in the 0° line at each momentum gave an estimated error of less than 0.5°, considering the size of the

special 0° beam defining counter and its distance from the center of the target.

C. Beam Momentum

1) The error in the momentum of the beam pion due to the dispersion in the beam was $\leq$ 1.5%.

2) The pions in the beam, transversing paths of differing length in the target before interacting, undergo different energy losses. Hence, there was a spread in their momenta of $\pm$4 MeV/c, or 0.4%. The momenta defining leg of the beam was set so as to give the quoted momenta at the center of the target, taking into account the energy losses due to material in the beam.

3) The error in the wire-orbiting of the momentum defining magnet was less than 1%.

Appendix D.

An Independent Check on the Polarization Parameter

An alternative method used to obtain the polarization parameter used the entire event sample (i.e., irregardless of γ-ray multiplicities), completely ignoring information on the detected γ-rays. Time-of-flight distributions using 0.2 ns bins were made for each counter and were characterized by higher statistics but lower signal-to-background ratios than the distributions used in the previous analysis. At each momentum there were three distributions, one for each sign of target polarization, and one for the dummy data. The time-of-flight distributions were characterized by a "prompt peak" (β=1), which corresponded to a triggering of the neutron counter by a γ-ray which failed to be detected by our veto system, and, for the polarized target data, a π^0 peak occurring at the time-of-flight τ_i^0 expected for neutrons from the reaction $\pi^- p \rightarrow \pi^0 n$ for the i^{th} counter, as well as background events extending over a wide range of times-of-flight.

A wide timing window was chosen about the time τ_i^0 (for each neutron counter N_i) to include most of the hydrogen events. The background events under the hydrogen "peak" were estimated by comparing the "tails" of the dummy and polarized target distributions and multiplying the dummy data in the region of the hydrogen peak with the normalization ratio so obtained. This determined the background used in the evaluation of the polarization parameter. The "tails" of the distributions were regions chosen far enough from the region of the hydrogen peak to ensure they consisted only of background events.

The polarization parameter, and its error, was evaluated for a series of different timing cuts (with the same timing cuts used for all three distributions). For simplicity, target polarizations of ±0.50 were used. The value of the polarization parameter so calculated was found to be insensitive to the particular timing cut chosen. The false asymmetries were checked as described previously and were found to be consistent with zero asymmetry. The polarization parameter was evaluated for regions in the "tails" of the polarized target data, and was found to be consistent with the hypothesis of zero asymmetry. This is very important, since polarization effects in the background would lead to incorrect values for the polarization parameter. A change of the background normalization of ±10% changed the values of the polarization parameter by less than one standard deviation.

All of the beam momenta except for 1245 MeV/c were analyzed in this way, with the results being in excellent agreement with the previously quoted values calculated using only two-shower events. 1245 MeV/c was troubled with target difficulties, with several different polarized targets being used during the run, making the background subtraction more difficult and less reliable. This method also allowed the calculation of the polarization parameter for the most forward neutron counter (the most backward scattering angle) which had very few two-shower events associated with it. The values quoted in the tables were obtained by this method, with the errors reflecting an additional error in the target polarization to compensate for the nominal values used in the calculation.

ACKNOWLEDGEMENTS

I would like to thank Herb Steiner, Gil Shapiro and Owen Chamberlain, under whose aegis I completed my graduate work, for their efforts in the design and execution of this experiment.

A great deal of the experimental training of the "experimental" physicist in this group is handled by Ray Z. Fuzesy, who taught me what I know of the arts and crafts of the polarized target, and a multitude of other things as well. His advice and encouragement, given to each graduate student in turn, is deeply appreciated.

Much of my early graduate work was in the company of Chuck Morehouse, Steve Rock, Thomas Powell, Peter Robrish and Bill Gorn, all of whom contributed greatly to my development as a physicist, and were remarkably good people to work with. The latter two deserve a special thanks for all of their help.

I am indebted to Bob Kenney, Mike Wahlig, Morris Pripstein, Jerry Nelson, Orin Dahl, Bill Oliver and Roger Chaffee for their help; indeed, their collaboration on this experiment was in large part responsible for its success.

I would like to thank Al Bridgewater, Randy Johnson, Lenny Anderson, Dave Pollard, John Jaros and Geoff O'Keefe for their careful work and their long hours at the helm.

The scanning, measuring and organization of the vast amounts of data from this experiment were taken care of by Ellen Epstein and Doug Stevenson, to whom I extend my appreciation.

I appreciate the help of Tim Daly and Mike Long throughout the experiment.

Thanks go to Jeanne Miller, who struggled with me through the typing of this thesis. A special note of thanks to Rosemary Fowell, who was a source of support and loyalty in my early days as a graduate student.

Jill Pipkin, Lynne Haroun and Susie Rosenstein all were a constant source of encouragement throughout the long years of this experiment, enjoying the ups, and suffering the downs along with me. To each of them my heartfelt thanks.

TECHNICAL INFORMATION DIVISION
LAWRENCE BERKELEY LABORATORY
UNIVERSITY OF CALIFORNIA
BERKELEY, CALIFORNIA 94720